3 Carbon Nanotubes and Bismuth Nanowires

Milded. S. Dresselhaus, Ado Jorio, and Oded Rabin

CONTENTS

3.1   INTRODUCTION

Carbon nanotubes and bismuth nanowires are both model systems for describing the one-dimensional properties of nanotubes and nanowires and will be discussed in this context in this chapter. For the case of carbon nanotubes, their one-dimensional aspects are best seen when they are prepared as single-wall carbon nanotubes (cylinders with walls one carbon atom in thickness) with approximately 1 nm diameters and lengths typically of about 10 μm. Their one-dimensional (1-D) properties are best exemplified in their 1-D electronic density of states (DOS), because their special physical properties are closely connected with their unique 1-D electronic DOS. The special properties associated with bismuth nanowires are closely connected to their unique semimetal to semiconducting transition, which occurs at approximately 50 nm wire diameter, now

making available the special properties of bismuth in the form of a semiconductor with highly anisotropic constant energy surfaces, effective mass components, and physical properties. This chapter focuses on the preparation and characterization of these materials.

For both of these systems, simple model calculations can be carried out to explain most of the unusual properties that are observed in their nanostructured form. These model calculations can be used to modify the conditions of their physical preparation to produce desired properties. Characterization of these materials is important to establish what their intrinsic properties are and how these basic properties can be used, controlled, or modified for both scientific studies and practical applications.

3.2 CARBON NANOTUBES

3.2.1 An Overview

The special interest in carbon nanotubes stems from their unique structure and properties, their very small size (as small as ~0.42 nm in diameter), the possibility for carbon nanotubes to be metallic or semiconducting depending on their geometric structure, their exceptional properties of ballistic transport, extremely high thermal conductivity, extremely high optical polarizability, and possibilities of high structural perfection. Single-wall carbon nanotubes (SWNTs) have only one atomic species (carbon) and have a relatively simple structure (a sheet of regular hexagons of carbon atoms rolled in a seamless way into a cylinder one atom thick). Single-wall nanotubes thus provide a benchmark for studying and characterizing new 1-D phenomena originating from their unique molecular density of states, whereby every structurally distinct (n,m) nanotube has its own unique and characteristic 1-D density of states, as discussed below. Many unexpected phenomena that do not occur in the parent graphite material have been discovered in carbon nanotubes and these discoveries have energized not only nanotube research, but also carbon and nanoscience research more broadly. Major gaps in basic knowledge remain, with the major obstacle confronting the carbon nanotube field being the lack of a detailed understanding of the nanotube growth mechanism. Such understanding is needed so that nanotubes of desired diameter and chirality can be grown in a monodispersed and controlled way because of the unusually close connection between nanotube properties (such as their metallicity, i.e., whether they are metallic or semiconducting) and their geometric structure. For this reason, much of current research effort is directed toward the synthesis and characterization of SWNTs.

There are basically three different methods used to grow single-wall carbon nanotubes (SWNTs): the arc discharge, laser vaporization, and chemical vapor deposition (CVD) methods.[1–3] The synthesis methods will be briefly described subsequently, after the uniqueness of each (n,m) nanotube is further clarified, where (n,m) denotes the structural indices used to characterize SWNTs.

Double-wall carbon nanotubes (DWNTs), consisting of two coaxial cylindrical SWNTs one inside the other as in a Russian doll arrangement, provide a prototype for studying the structure and properties of multiwall carbon nanotubes (MWNTs) in a quantitative way. Because of the increased stability and durability of DWNTs

and MWNTs relative to SWNTs, these more robust DWNTs and MWNTs are expected to have more potential for applications, exploiting the exceptional mechanical strength and stiffness and the very high thermal conductivity of carbon nanotubes.[4] Before discussing the synthesis and characterization of SWNTs and DWNTs, the unique aspect of (*n*,*m*) nanotubes is presented so that the synthesis and characterization of nanotubes can be discussed in a proper framework.

Since every structurally distinct (*n*,*m*) nanotube can be considered to be a distinct molecule, it is important to provide the framework used to distinguish one nanotube from another. As illustrated in Fig. 3.1, a single-wall carbon nanotube is geometrically just a rolled-up graphene sheet. Its structure can be specified or indexed by its circumferential periodicity ($\vec{C}_h$), as described using the chiral vector (*AA′* in Fig. 3.1), which connects two crystallographically equivalent sites (*A* and *A′*) on a graphene sheet. In this way, the geometry of each SWNT is completely specified by a pair of integers (*n*,*m*) denoting the relative position $\vec{C}_h = n\vec{a}_1 + m\vec{a}_2$ of the pair of atoms on a graphene strip that, when rolled onto each other, form a tube. Here $\vec{a}_1$ and $\vec{a}_2$ are basis vectors of the hexagonal honeycomb lattice, as shown in Fig. 3.1. This chiral vector $\vec{C}_h$ also defines a chiral angle θ, which is the angle between $\vec{C}_h$ and the $\vec{a}$ direction of the graphene sheet. For the tubes with (*n*,0), called zigzag tubes, and the tubes with (*n*,*n*), called armchair tubes,[5] the translation and rotation symmetry operations are independent (and these tubes form symmorphic space groups), while for all other (*n*,*m*) tubes, the rotations and translations are coupled (nonsymmorphic space groups).[5] The assembly of MWNTs follows a Russian doll arrangement with the stacking of tubes coaxially at an interlayer distance of greater than about 0.34 nm, which is the interlayer separation of turbostratic graphene layers that lack the ABAB . . . interlayer stacking order found in 3-D graphite. There does not seem to be a correlation between the (*n*,*m*) on one layer and the (*n′*,*m′*) of the adjacent layers beyond a preference for minimizing
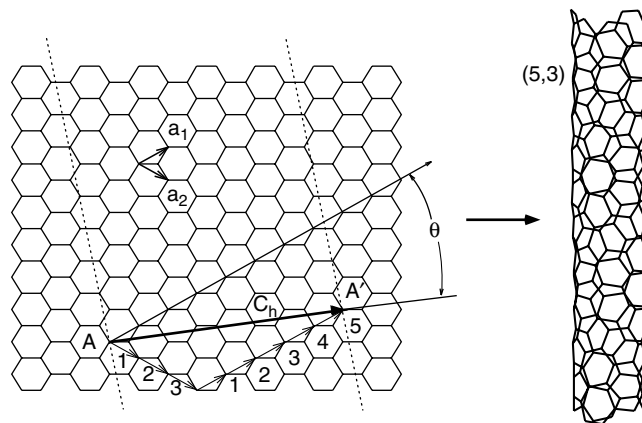

FIGURE 3.1 Schematic diagram showing a possible wrapping of the two-dimensional graphene sheet into a tubular form. In this example, a (5,3) nanotube is under construction and the resulting tube is illustrated on the right.[6]

the interlayer separation to be as close as possible to the turbostratic interplanar distance to maximize the coupling between adjacent SWNTs.

Before the first SWNT was ever synthesized in the laboratory, theoretical calculations[7–9] showed that the electronic properties of SWNTs are very sensitive to their geometric structure. Although graphene (2-D graphite) is a zero-gap semiconductor,[5] theory predicted that carbon nanotubes can be metals or semiconductors with different-size energy gaps, depending very sensitively on the indices (n,m) or equivalently on the diameter and helicity of the tubes. In addition, each chiral (n,m) nanotube ($0 < \theta < 30°$) also has a distinct handedness that further defines its uniqueness.[10]

The physics behind this sensitivity of the electronic properties of carbon nanotubes to their structure can be understood by relating the nanotube electronic structure to that of the graphene sheet that is rolled to produce the SWNT. The unique band structure of a graphene sheet shown in Fig. 3.2 has states crossing the Fermi level at only one point in k-space, denoted by the point K in Fig. 3.2. The quantization of the electron wave-vector along the circumferential direction resulting from the periodic boundary conditions leads to the formation of energy subbands associated with cutting lines $k_\perp = \mu K_1$ separated from one another by a distance $K_1 = 2/d_t$. The d_t is the nanotube diameter, μ is an integer denoting each quantum state in the circumferential direction for each cutting line, and a quasicontinuum of states k_{11}, described by a reciprocal lattice vector K_2 occurs along the length of such cutting lines.[11] The K_1 and K_2 reciprocal lattice vectors form the basis vectors of the nanotube Brillouin zone.

An isolated sheet of graphite is a zero-gap semiconductor whose electronic structure near the Fermi energy is given by an occupied π band and an empty π^* band.
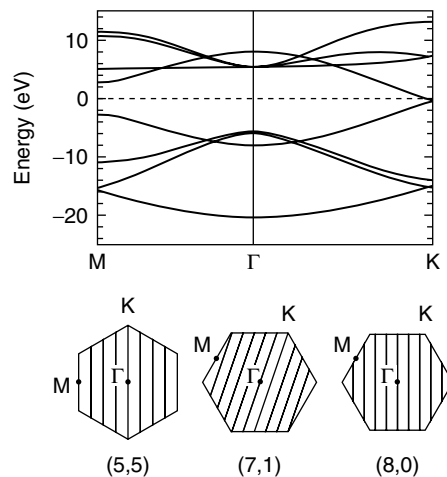

FIGURE 3.2 (Top) Tight-binding band structure of graphene (a single basal plane of graphite), showing the π and σ bands in the main high symmetry directions. (Bottom) Allowed $\bar{k}$-vectors of the (5,5), (7,1), and (8,0) tubes (solid lines) mapped onto the graphite Brillouin zone.[6]

These two bands have a linear dispersion $E(k)$ around the K point in the Brillouin zone and, as shown in Fig. 3.2, they meet at the Fermi level at the K point. The Fermi surface of an ideal graphite sheet consists of the six corner K points. The allowed set of k's in SWNTs, indicated by the lines in Fig. 3.2, depends on the diameter and helicity of the tube. Whenever the allowed k's include the point K, the system is a (1-D) metal with a nonzero density of states at the Fermi level, resulting in a one-dimensional metal with two linear dispersing bands. When the point K is not included in the set of allowed states, the system is a semiconductor with different-size energy gaps depending on both d_t and θ. The d_t dependence comes from the $K_1 = 2/d_t$ relation, and the θ dependence comes from the fact that the equi-energies around the K point are not circles, but they exhibit a trigonally warped shape[5]. It is important to note that the states near the Fermi energy for both metallic and semiconducting tubes are all from states near the K point, and hence their transport and other electronic properties are related to the properties of the states on the cutting lines, with the conduction band and valence band states of a semiconducting tube coming from states along the cutting line closest to the K point.

The general rules coming from symmetry considerations tell us that SWNTs come in three varieties: armchair (n,n) tubes, which are always metals; (n,m) tubes with $n - m = 3j$, where j is a nonzero integer, which are very tiny-gap semiconductors, but they behave like metals at room temperature; and large-gap semiconductors for which $n - m = 3j \pm 1$ (Fig. 3.3). As the tube diameter d_t increases, the band gaps of the large-gap and tiny-gap varieties decrease with a $1/d_t$ and $1/d_t^2$ dependence, respectively. The $1/d_t^2$ dependence for the tiny gap is due to a curvature effect and depends on chiral angle, the tiny gap being a maximum for zigzag and zero for armchair SWNTs. Thus, in Fig. 3.2, a $(7,1)$ tube would be metallic at 300 K, whereas a $(8,0)$ tube would be semiconducting, while the $(5,5)$ armchair tube would always be metallic, consistent with whether or not a cutting line goes through the K point of the 2-D Brillouin zone. The corresponding electronic density of states for these three SWNTs are shown in Fig. 3.3. The main point to be emphasized is that the energy eigenvalues for every (n,m) SWNT are unique, and therefore each (n,m) nanotube is considered a distinct molecule with potentially different properties. Van Hove singularities (vHSs), characteristic of the density of states for 1-D systems, are found for both semiconducting and metallic SWNTs. To the extent that a specific application, such as for an electronic device, depends on the distinction between different (n,m) tubes, the synthesis of SWNTs depends on a high degree of control of the synthesis process discussed in the next section.

3.2.2 NANOTUBE SYNTHESIS

All three synthesis methods [arc discharge, laser vaporization, and chemical vapor deposition (CVD)] produce carbon atoms in a hot gaseous form by evaporation from a condensed phase and these highly energetic carbon atoms then reassemble themselves to form carbon nanotubes. All methods use nanosize catalytic particles to induce the synthesis process and to control the diameter of the nanotubes that are synthesized. For the arc and laser methods, carrier gases are used for transporting nanotubes from where they are formed in the reactor to where they are collected,
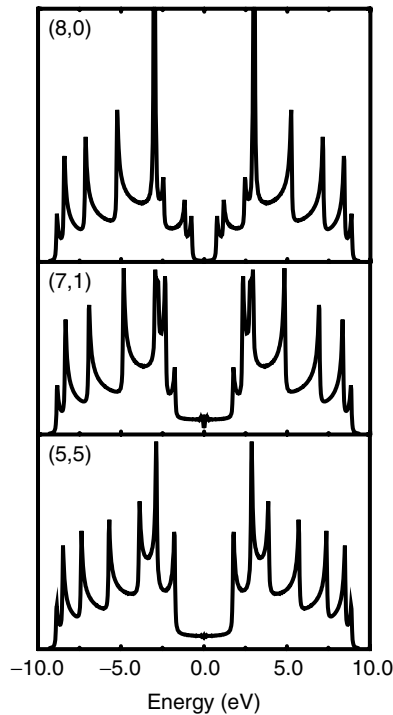
FIGURE 3.3 Electronic densities of states for the (5,5), (7,1), and (8,0) SWNTs showing singularities characteristic of 1-D systems. The (5,5) armchair nanotube is metallic for symmetry reasons, with a constant energy-independent density of states between the first singularities in the valence and conduction bands. The (7,1) chiral tube displays a tiny band gap due to curvature effects, but will display metallic behavior at room temperature. The (8,0) zigzag tube is a large-gap semiconductor.[12]

clearing the way for the subsequent growth of SWNTs in the more active reaction region of the reactor.[13] The arc-discharge[14,15] and laser ablation[16] methods were the first methods to allow gram quantities of SWNTs to be synthesized, and these methods are still used today, as a source of high-quality samples for specific fundametal studies. However, the chemical vapor deposition (CVD) method is the method most amenable for large-scale production of SWNTs. The HiPco (high pressure catalytic decomposition of carbon monoxide) adaptation of the CVD approach uses floating catalytic particles and is a common commercial source of SWNTs for both research and applications use.[17] However, the adaptation of the CVD process based on alcohol[18] produces relatively clean SWNT bundles with fewer residual catalytic particles, and when operated at relatively low temperatures (e.g., ~650°C), smaller diameter tubes are favored.[19] Common catalytic particles are Mo, Co, Fe, but alloys of Co-Mo and Fe-Co have been found to produce high SWNT yields. Use of Co-Mo bimetallic catalysts and a fluidized bed CVD reactor in a CoMoCAT process[20,21] has been especially successful in the efficient production of small-diameter SWNTs.

Right now rapid progress is being made on nanotube synthesis to increase the control of the synthesis process, steadily narrowing the diameter and chirality range of the nanotubes that are produced, decreasing their defect and impurity content, increasing their production efficiency and yield, while expanding the functionality of nanotubes. The main directions in the pursuit of controlled nanotube synthesis include the synthesis of molecular catalytic clusters with atomically well-defined size and shape, the development of mild catalytic synthesis conditions at reduced temperatures, the development of patterned growth with a high degree of control in nanotube location and orientation, and the synthesis of complex and organized networks or arrays of nanotubes on substrates.[13]

Much attention is also being given to the synthesis of multiwall carbon nanotubes (MWNTs) and double-wall carbon nanotubes (DWNTs) because of their attractiveness for specific applications where mechanically robust nanostructures are needed. Here DWNTs can be considered a model system because of their similarity in physical properties to MWNTs and their relative simplicity. The synthesis of double-wall nanotubes can be accomplished either in a direct synthesis process or from a SWNT whose core has been previously filled with C_{60} molecules by a gas phase reactor at ~400°C on an acid-purified open-ended SWNT bundle. The transformation of the C_{60}-filled SWNTs (called peapods) to DWNTs is accomplished by heat treatment in the temperature range 800–1200°C.[4]

Typically the growth of single-wall carbon nanotubes usually involves a catalytic process, with nanotubes grown in the presence of catalytic particles, but these growth conditions typically produce a variety of other carbon species, and many other unwanted constituents. Therefore, much attention has also been given to nanotube purification from other species, techniques for the characterization of nanotube purity, and for the preparation/sorting of nanotubes by length, diameter, chirality, and metallic/semiconducting properties and perhaps other attributes.[22] Chemical methods are generally used for the removal of metal particles and other unwanted impurities[23–26] and high-temperature heat treatment in vacuum can be used to remove structural defects such as heptagon-pentagon pairs.[26,27]

Nanotube synthesis and purification are closely connected from two points of view. First an improvement in the synthesis process regarding purity and monodispersity in tube diameter and chirality would reduce the need for extensive post-synthesis purification and separation. Second, if efficient and precise purification and separation techniques can be developed, the stringent limit that the growth process should produce a single (n,m) species could perhaps be relaxed. The convergence or combination of the two approaches, that is, the controlled or preferential growth of a particular (n,m) nanotube, and an effective and easy purification/separation process[4] could prove powerful in producing nanotubes with well-defined diameters and chiralities.

It is well known that SWNTs can be either semiconducting or metallic depending on their geometry (see Section 3.2.1). At present, all known synthesis processes yield a mixture of semiconducting and metallic SWNTs within a single SWNT bundle. For DWNTs or MWNTs, the various shells will contain a random collection of semiconducting (S) and metallic (M) constituents with an approximate 2:1 ratio expected for $S:M$ tubes, assuming equal a-priori probability for occurrence, which

is realized when many different (*n,m*) constituents are present in the sample. Nanotube applications in some cases, such as electronics, require control of the synthesis process to discriminate between *S* and *M* SWNTs, and for circuit applications, control of diameter and chirality could also be required. Such control of the synthesis process will be a research challenge of the future.

For the present, effort is also being given to the separation of SWNTs into *M*-enriched and *S*-enriched samples by a variety of processes, which preferentially distinguish *S* tubes from *M* tubes. One of these separation processes is attributed to the enhanced chemical affinity of the octadecylamine (ODA) surfactant for *S* SWNTs dispersed in tetrahydrofuran (THF), rendering *M* SWNTs more prone to precipitation when the THF is partially evaporated, leaving behind a supernatant that is enriched in *S* SWNTs.[28] Another separation procedure for enriching *M* or *S* SWNTs is based on ion-exchange liquid chromatography of DNA-assisted SWNT solubilization, relying on the lower negative charge density of DNA-*M* SWNT hybrids. In this process, *M* SWNT–enriched fractions elute before *S* SWNT– enriched fractions.[29,30] More recently the separation of *M* from *S* SWNTs using alternating current dielectrophoresis in an aqueous SWNT suspension was achieved, making use of the higher induced dipole moment of *M* SWNTs.[31] And even more recently selective functionalization of *M* SWNTs against *S* SWNTs after addition of 4-chlorobenzenediazonium tetrafluoroborate to an aqueous suspension of SWNTs was reported, based on the higher activity of covalent aryl bonds of diazonium with *M* SWNTs than with *S* SWNTs.[32–34] *M/S* separation has also been reported using centrifugation of a surfactant-stabilized aqueous suspension of SWNTs with the addition of diluted bromine. Here *M* SWNTs form more highly structured charge-transfer complexes with bromine than *S* SWNTs, thereby yielding an excess of *M* SWNTs in the supernatant and of *S* SWNTs in the sediment.[35]

The development of many different separation procedures demands that a simple and reliable method be developed for the quantitative evaluation of the separation efficiency. Several optical techniques widely used in nanotube science can provide such a characterization tool. Optical absorption spectroscopy[36] is one suitable candidate for the characterization process of the separated samples once the individual peaks in the absorption spectra are assigned to *M* and *S* SWNTs,[37] as discussed in Section 3.2.5. Such measurements are difficult to quantify, because the most intense optical peak is strongly influenced by exciton effects and because the intensity of all of the optical absorption peaks are not only influenced by the number density of the *M* and *S* species but by their oscillator strengths for each of the optical transitions. Resonance Raman spectroscopy (RRS)[38] provides an alternative for the characterization of *M*- and *S*-enriched aliquots, since *M* and *S* SWNTs yield distinct features in the resonance Raman spectra, as discussed in Section 3.2.4.[39] With the RRS technique, the intensity of the radial breathing mode peaks are likewise influenced by the strength of the matrix elements for the Raman intensity. The pertinent matrix elements for the Raman effect include the electron-photon and electron-phonon matrix elements. In addition, Raman spectra have to be taken at a sufficient number of laser excitation energies to get a good sampling of the SWNTs present in the sample. Photoluminescence would be useful in making a determination of how the diameter distributions change during the separation process, but it is less useful in

evaluating the *M* and *S* separation, since *M* SWNTs show no luminescence and, furthermore, the presence of *M* SWNTs in a nanotube sample quenches the luminescence from *S* SWNTs by sharply reducing the lifetime of the excited states of the *S* SWNTs through nonradiative decay pathways.[40]

3.2.3 NANOTUBE CHARACTERIZATION

There are a number of methods used to characterize the structure and properties of both individual nanotubes and nanotube bundle samples. In this section, general characterization approaches are discussed while in Section 3.2.4 the characterization of SWNTs by Raman spectroscopy is discussed in some detail.

One obvious method to determine whether a SWNT is metallic or semiconducting would be to measure its electrical conductivity. Such measurements can be done, but they are not easy to carry out quantitatively because of the small size of the SWNT diameter and the difficulty in making reproducible electrical contacts. Transport measurements, however, are not useful for specific (*n,m*) identification.

In practice, electron microscopy has been widely used for structural characterization. Scanning electron microscopy (SEM) is routinely used to evaluate the morphology and the amount of remaining catalytic particles and other carbon forms present in an as-prepared SWNT sample, while an EDAX (energy dispersive x-ray analysis) attachment is typically used for the chemical detection of the non-carbon species present in the sample and their relative concentrations. Transmission electron microscopy (TEM) is used to image the lattice planes to evaluate the structural perfection of the sidewalls of an individual SWNT. Imaging is also used to study the cap structure of SWNTs and MWNTs, as well as to study the bamboo structure of the inner tubes of a MWNT. For SWNTs, the TEM is commonly used to obtain electron diffraction patterns, and from these patterns to determine the (*n,m*) indices for an individual SWNT.

Scanning probe microscopy (SPM) has been used to characterize isolated SWNTs spread on surfaces. Atomic force microscopy (AFM) has been widely used to the measure the diameters of individual SWNTs, while low temperature, atomic resolution scanning tunneling microscopy (STM) images can be used to measure the chiral angles of individual SWNTs. In the scanning tunneling spectroscopy (STS) mode, a scanning probe instrument can be used to measure (*I/V*) *(dI/dV)* for individual SWNTs, thereby yielding scans of the electronic density of states from which the (*n,m*) indices for individual SWNTs can be determined.

Optical techniques, including optical absorption, photoluminescence, and Raman scattering have been widely used to characterize carbon nanotubes by studying both their electronic and phonon (lattice bibrational) spectra. These methods have the advantage of not requiring contacts and in being a very weakly perturbing probe. In Section 3.2.4, Raman spectroscopy, which is the most widely used spectroscopic tool for nanotube characterization is discussed in some detail, while in Section 3.2.5 other photophysical techniques are briefly reviewed.

3.2.4 RAMAN SPECTROSCOPY

The Raman spectra of SWNTs have been particularly valuable for providing detailed information for characterizing SWNT samples,[38] and several of the features in the
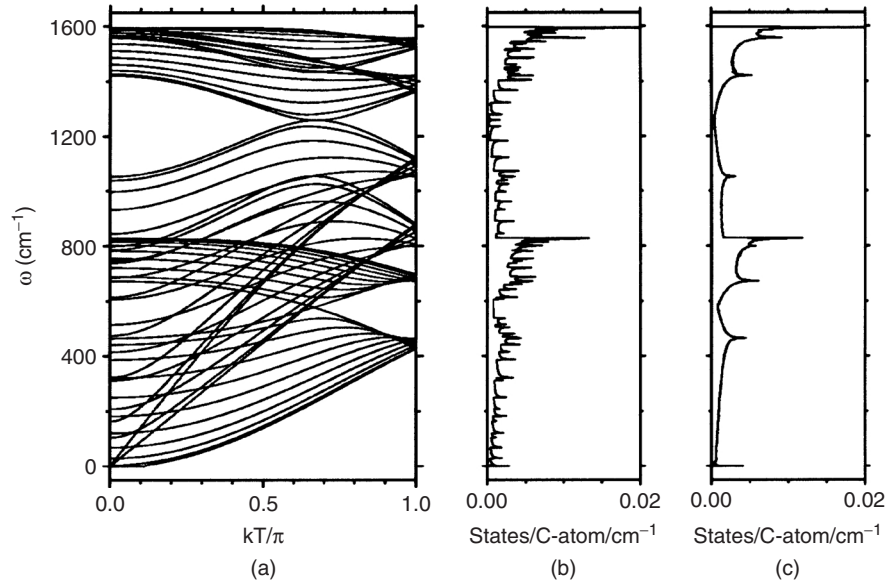
FIGURE 3.4 (a) The calculated phonon dispersion relations of an armchair carbon nanotube with $(n,m) = (10,10)$, for which there are 120 degrees of freedom and 66 distinct phonon branches.[5] (b) The corresponding phonon density of states for a (10,10) nanotube. (c) The corresponding phonon density of states for a 2-D graphene sheet, shown for comparison.[5]

Raman spectra have been used for SWNT characterization, as indicated below. In the first report of Raman spectra from SWNTs,[38] it was shown that despite the large number of branches in the SWNT phonon dispersion relations (Fig. 3.4(a)), the Raman spectra for a SWNT bundle (Fig. 3.5) exhibit only two dominant features, namely the radial breathing mode (RBM), which in this trace appears at 186 cm^{-1} for a laser excitation energy $E_{laser} = 2.41$ eV, and the tangential band for vibrations along the surface of the SWNT appears in the range of 1520–1620 cm^{-1}. Because of the strong connection of this tangential band to the corresponding mode in 2-D graphite, this higher frequency band for SWNTs is commonly called the *G*-band. Other lower intensity features, seen in Figs. 3.5 and 3.6 and discussed below, also provide important and unique information about SWNTs.

In this first paper on the Raman effect in SWNTs,[38] the strong and nonmonotonic dependence of the SWNT Raman spectra on the laser excitation energy E_{laser} established the Raman scattering to be a resonance process occurring when E_{laser} matches the optical transition energy E_{ii}, between van Hove singularities in the valence band and conduction bands (Fig. 3.3). Raman scattering in SWNTs is very important for the characterization of SWNTs because it relates the photon excitation directly to both phonon and electron processes in SWNTs. Since the E_{ii} value for a particular SWNT is dependent on its diameter d_t, so are the Raman spectra that are observed. Because of the very small diameters of SWNTs (~1 nm), the joint density of states exhibits very large singularities, with associated large enhancements in Raman intensity,
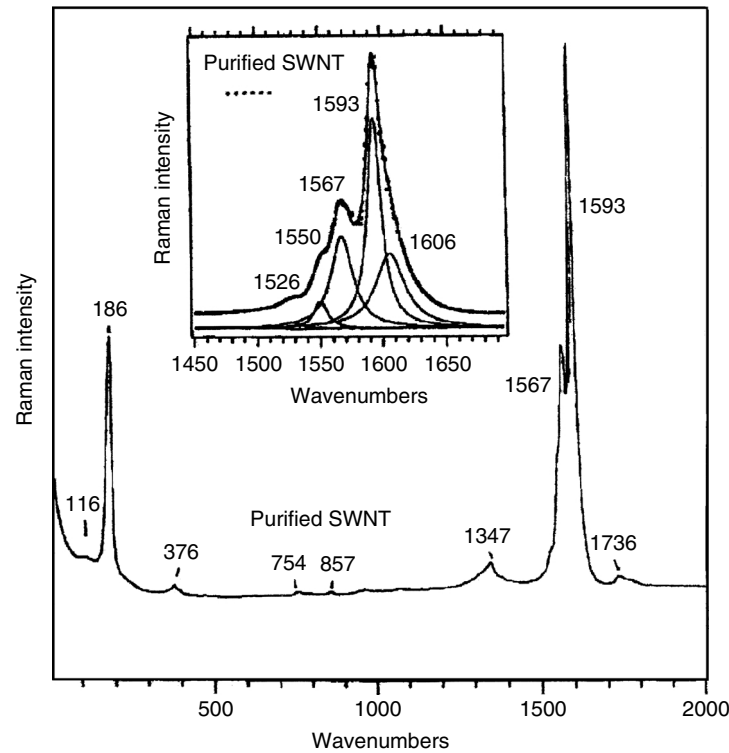
FIGURE 3.5 Experimental Raman spectrum taken with 514.5 nm (2.41 eV) laser excitation from a SWNT bundle sample with a diameter distribution $d_t = 1.36 \pm 0.20$ nm. The inset shows an expanded version of the spectra in the 1450–1700 cm^{-1} range, fit by a sum of Lorentzians.[38]

allowing the observation of spectra from an individual SWNT that is in strong resonance with E_{laser}.[41] From the point of view of nanotube characterization, the resonance Raman effect allows the selection for detailed examination of only the few SWNTs in a sample that are in resonance with a given E_{laser}. For example, the RBM for which all carbon atoms in a given nanotube are vibrating in phase in the radial direction has a frequency ω_{RBM} that is highly sensitive to the nanotube diameter, as discussed below, thereby providing information on both the mean diameter and the diameter distribution of a particular SWNT sample.[42]

Figure 3.5 indicates that the *G*-band feature consists of a superposition of two dominant components, shown at 1593 cm^{-1} (G^+) and at 1567 cm^{-1} (G^-) (see the inset to Fig. 3.5), although the G^- component exhibits a weak diameter dependence. The G^+ feature is associated with carbon atom vibrations along the nanotube axis and its frequency ω_{G^+} is sensitive to charge transfer from dopant additions to SWNTs (upshifts in ω_{G^+} for acceptors, and downshifts for donors). The G^- feature, in contrast, is associated with vibrations of carbon atoms along the circumferential direction of the nanotube, and its line-shape is highly sensitive to whether the SWNT is metallic
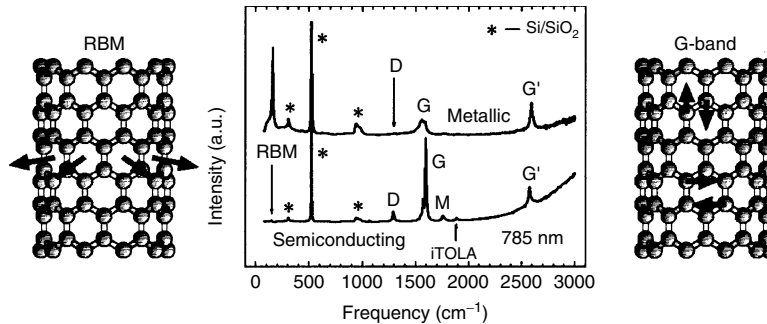
FIGURE 3.6 Raman spectra from a metallic (top) and a semiconducting (bottom) SWNT at the single nanotube level using 785 nm (1.58 eV) laser excitation, showing the radial breathing mode (RBM), *D*-band, *G*-band, and *G*′ band features, in addition to weak double resonance features associated with the *M*-band and the iTOLA second-order modes. Insets on the left and the right show, respectively, atomic displacements associated with the RBM and *G*-band normal mode vibrations. The isolated carbon nanotubes are sitting on an oxidized silicon substrate that provides contributions to the Raman spectra denoted by ∗, which are used for calibration purposes.

(Breit–Wigner–Fano line-shape) or semiconducting (Lorentzian line-shape).[43,44] All-in-all there are six modes contributing to the *G*-band, with two each having A, E_1, and E_2 symmetries, and each symmetry mode can be distinguished from the others by its behavior in polarization-sensitive Raman experiments.[45] The features of highest intensity are the G^+ and G^- features of A symmetry, and it is these components that are normally used to characterize carbon nanotubes with regard to their metallicity and involvement in charge transfer. Polarization studies on SWNTs are best done at the single-nanotube level.[46]

Also commonly found in the Raman spectra in SWNT bundles are the *D*-band (with ω_D at 1347 cm^{-1} in Fig. 3.5), stemming from the disorder-induced mode in graphite, and its second harmonic, the *G*′ band (Fig. 3.6) occurring at ~$2\omega_D$. Both the *D*-band and the *G*′-band are associated with a double resonance process,[47] and are sensitive to the nanotube diameter and chirality. The large dispersion of the *D*-band and *G*′-band features have been very important in revealing detailed information about the electronic and phonon properties of SWNTs as well as of the parent material graphite.[48–50]

Because of the sharp van Hove singularities occurring in carbon nanotubes with diameters less than 2 nm, the Raman intensities for the resonance Raman process can be so large that it is possible to observe the Raman spectra from one individual SWNT,[41] as shown in Fig. 3.6, where the differences in the *G*-band spectra between semiconducting and metallic SWNTs can be seen at the single nanotube level. Because of the trigonal warping effect, whereby the constant energy contours in reciprocal *k* space for 2-D graphite are not circles but show threefold distortion, every (*n*,*m*) carbon nanotube has a different electronic structure and a unique density of states (Fig. 3.3). Therefore the energies E_{ii} of the van Hove singularities in the
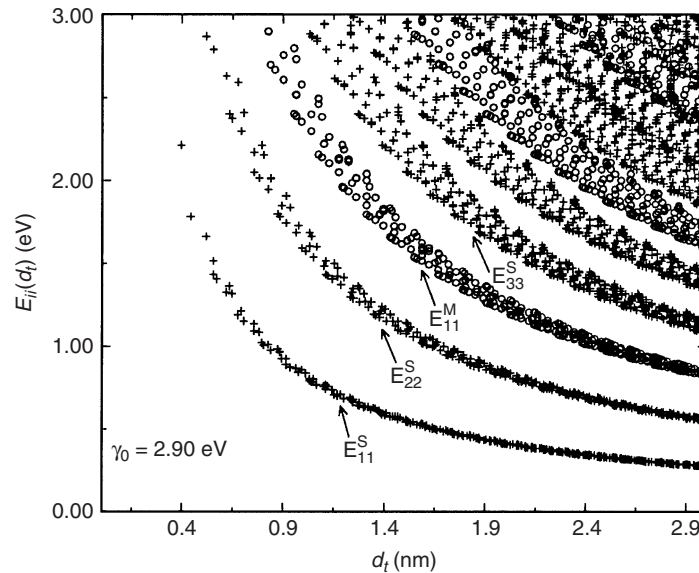
FIGURE 3.7 Calculated[51] energy separations E_{ii} between van Hove singularities i in the 1-D electronic density of states of the conduction and valence bands for all possible (n,m) values vs. nanotube diameter in the range $0.4 < d_t < 3.0$ nm, using a value for the carbon–carbon energy overlap integral of $\gamma_0 = 2.9$ eV and a nearest neighbor carbon–carbon distance $a_{C-C} = 0.142$ nm for making this plot.[49,58] Semiconducting (S) and metallic (M) nanotubes are indicated by crosses and open circles, respectively. The subscript $i = 1$ denotes the index of the lowest energy of a singularity in the joint density of states.

joint density of states for each SWNT (as shown in Fig. 3.4(b) and calculated, for example, by the tight binding approximation) are different, as shown in Fig. 3.7, where the E_{ii} ($i = 1, 2, 3, \ldots$) values for all (n,m) nanotubes in the diameter range up to 3.0 nm are shown for E_{ii} up to 3.0 eV.[51] In this so-called Kataura plot (Fig. 3.7), we see that for small-diameter SWNTs ($d_t < 1.7$ nm) and for the first few electronic transitions for semiconducting and metallic SWNTs, the E_{ii} values are arranged in bands, whose widths are determined by the trigonal warping effect[49] so that if there were no trigonal warping, the spread in energy at constant diameter would go to zero. A general chiral semiconducting SWNT will have van Hove singularities in the $E_{11}^{S}, E_{22}^{S}, E_{33}^{S}, \ldots$ bands, while a chiral metallic SWNT will have two vHSs in each of the $E_{11}^{M}, E_{22}^{M}, \ldots$ bands. The tight binding approximation provides predicted values for the E_{ii} energies for the vHSs for SWNTs with diameters in the 1.1–2.0 nm range (to an accuracy of better than 20 meV).[52] This Kataura plot can be used to estimate the appropriate laser energy that could be used to resonate with a particular (n,m) SWNT.

The Raman effect furthermore provides a determination of E_{ii} values, either by measurement of the relative intensities of the radial breathing mode for the Stokes (phonon emission) and anti-Stokes (phonon absorption) processes, or by

measurements of the RBM Raman intensity for the Stokes process for a particular (n,m) SWNT relative to the intensity for many SWNTs measured under similar conditions.[39] The frequency of the RBM has been used to determine the diameter of an isolated SWNT sitting on an oxidized Si surface, using the relation ω_{RBM} $(\text{cm}^{-1}) = 248/d_t$ (nm), which is established by measurements on many SWNTs. Moreover, from a knowledge of the (E_{ii}, d_t) values for an individual SWNT (Fig. 3.7), the (n,m) indices for that SWNT can be determined from the Kataura plot. Resonance Raman spectroscopy at the single-nanotube level can not only determine the (n,m) indices from study of the RBM frequency and intensity, but can also determine E_{ii} values for individual SWNTs to about 10 meV accuracy, using a single laser line or to about 5 meV accuracy using the Stokes–anti-Stokes intensity analysis method.[39] Resonance Raman measurements with a tunable laser system can give E_{ii} values with an accuracy of ± 3 meV.[53,54] The precision for this assignment using Stokes vs. anti-Stokes Raman measurements depends on the determination of the shape of the resonance window (Raman intensity as a function of excitation laser energy E_{laser}). The resonance window could change for samples with different environments, and with different sample preparation methods, and systematic work is still needed to increase the precision. The ability to use a gate,[55] an externally applied potential,[56] or a tunable laser[53,54,57] to move the van Hove singularity for an individual SWNT into and out of resonance with the laser offers great promise for future detailed studies of the 1-D physics of single-wall carbon nanotubes using resonance Raman spectroscopy. The ability to characterize individual SWNTs for their (n,m) identification allows the determination of the dependence on nanotube diameter and chirality of many physical phenomena in SWNTs that can be measured at the single-nanotube level.

Near field microscopy has also proven to provide a powerful tool for examining the Raman spectra on a spatially resolved basis (to 20 nm resolution), thus providing detailed information of the effect of specific defects on the vibrational spectra. The disorder-induced D-band provides a sensitive probe of symmetry breaking-agents such as defects in carbon nanotubes.[59,60]

Raman spectra of carbon nanotubes, particularly at the single-nanotube level, have been especially rich. Because of the simplicity of the geometrical structure of nanotubes, detailed analysis of the Raman spectra have yielded much information about the phonon dispersion relations, such as information about the trigonal warping effect for phonons. Such information was not yet available for 2-D graphite, but can now be studied in nanotubes because of their one-dimensionality.[50] Because of the close coupling between electrons and phonons under resonance conditions, Raman spectra have also provided valuable and detailed information about the electronic structure (such as an evaluation of the magnitude of the trigonal warping effect for electrons[48]), thus yielding valuable information about the electronic structure that can be used in the characterization of nanotube samples. At present, the use of many laser lines (over 50) provides the capability of carrying out Raman spectroscopy measurements with a quasicontinuous excitation energy source.[54,57] This capability promises to provide a means to access essentially all the SWNTs in a given sample, thereby providing a powerful new characterization technique for SWNTs.

3.2.5 OTHER PHOTOPHYSICAL TECHNIQUES

Optical absorption measurements on carbon nanotube samples generally show broad peaks[61] corresponding to E_{11}^S, E_{22}^S, and E_{11}^M with decreasing intensity as the energy increases, as expected from the f-sum rule for optical matrix elements.[62] These peaks are characteristic of SWNTs and provide one of the most important characterization techniques to distinguish nanotubes from other carbonaceous species in an unpurified sample containing nanotubes in the presence of other carbonaceous species. The characterization measurement is carried out by comparing the absorption intensity of the E_{22}^S band relative to the background absorption in the same range of the infrared spectra. The E_{22}^S peak is selected because it is relatively strong and is not expected to be strongly perturbed by excitonic effects, as is the E_{11}^S peak. Optical absorption spectra are not only used for the characterization of such mixed samples but as an aid in the purification of such samples to isolate the nanotubes from other species.[22,63]

Whereas optical absorption techniques can be used to characterize almost any type of sample containing carbon nanotubes, optical emission as a characterization tool require a specially prepared nanotube samples with sufficiently long carrier lifetimes in the excited state, so that the emission process has suffcient intensity to be observable,[40] as discussed in the next paragraph.

Time-domain photoemission studies using fast-optics provide information about the lifetime and electron-phonon matrix elements for the excited states. Time-domain studies on SWNT bundles have been performed, giving a measure of the lifetime of photoexcited charge-carriers in SWNT ropes as a function of electron energy (Fig. 3.8).[64,65] The lifetime of electrons excited to the π^* bands is found to decrease
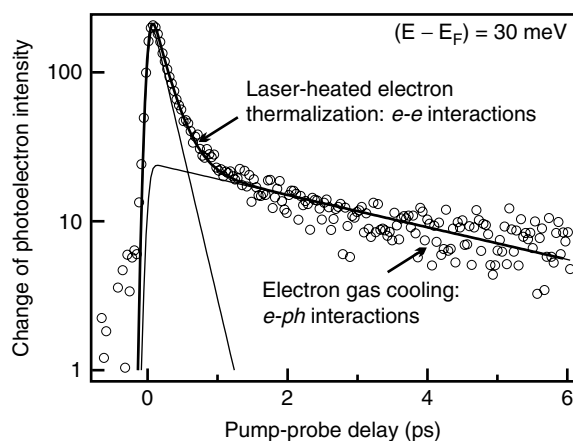

FIGURE 3.8 Time dependence of the photoelectron intensity during and after femtosecond-laser generation of hot electrons in SWNT bundles.[65] Electrons monitored by this trace are 30 meV above the Fermi level. The fast and slow components, respectively, correspond to internal thermalization of the laser-heated electron gas and to its equilibration with the lattice, i.e., by cooling.

continuously from 130 fs at 0.2 eV down to less than 20 fs at energies above1.5 eV with respect to the Fermi level.[64] These short lifetimes lead to a significant lifetime-induced broadening of the characteristic vHSs in the density of states, so that the optical effects related to the confinement of electrons into vHSs are stronger for the lower energy vHSs in the joint density of states. Experimental results show very similar excited-state decay times for graphite and SWNT bundles, suggesting that electron-electron scattering of photoexcited carriers in SWNT bundles may lead to a rapid charge transfer between different tubes, thus allowing excited electron-hole pairs in semiconducting SWNTs to relax almost as rapidly as those in metallic tubes. This result probably explains why photoluminescence is not observed for SWNT bundles.[40] The presence of conduction electrons in metallic tubes provides an effective nonradiative decay channel for the decay of photoexcited electrons. Thus to obtain photoluminescence spectra, the SWNTs contained in SWNT bundles need to be isolated from one another to reduce the nonradiative decay channel, and this has been done by the use of various species to wrap around individual SWNTs within a bundle to isolate individual SWNTs from each other. Some wrapping agents that have been effectively used include sodium dodecyl sulfate (SDS)[40,66] and single-stranded guanine-thyamine selected DNA chains (ss-GTDNA).[29]

The observation of photoluminescence (PL) from isolated SWNTs has made possible the observation of the E_{11}^S energy gap for semiconducting SWNTs, and interesting 3-D plots can be constructed (Fig. 3.9) showing strong intensity peaks for excitation of the electrons at E_{22}^S and emission at E_{11}^S, where each peak is related to one specific (n,m) SWNT. From this intensity plot in Fig. 3.9, a plot of the E_{11} and E_{22} electronic transition energies for many (n,m) SWNTs can be constructed.[66] By using an empirical expression for E_{ii} as a function of nanotube diameter and chiral angle for isolated SWNTs grown by the HiPco process, wrapped with SDS surfactant[67] and dispersed in aqueous solution, an assignment of the PL peaks with specific (n,m) values has been made. This assignment is based on the identification of families with ($2n + m$) = constant, which becomes increasingly evident as the SWNT diameter decreases and curvature effects become more important. The widths of the PL peaks are ~25 meV, corresponding to room temperature thermal energy.[37,40,66,67] The strength of the PL characterization technique is that all the (n,m) semiconducting tubes in the sample are probed at once so that, in principle, their relative concentrations could be determined (if the matrix elements and lifetimes for the (n,m) emissions were known theoretically) from the measured intensities of each PL peak.

The limitation for the photoluminescence method is related to systems where nonradiative electron-hole recombination can occur, so that light emission from metallic SWNTs or SWNT in bundles cannot be observed. For such samples, resonance Raman experiments at the single-nanotube level could be alternatively used. Raman measurements on SDS wrapped SWNTs in solution yield good agreement with E_{22}^S values obtained by PL measurements[54] within the accuracy of the PL measurements, which can only be made to 25 meV because of the broad line widths. In contrast, by using many laser lines, the accuracy of the E_{22}^S values is much greater (to 5 meV) as determined by resonance Raman spectroscopy, through measurement of both the Stokes and anti-Stokes RBM features, as discussed in Section 3.2.4.
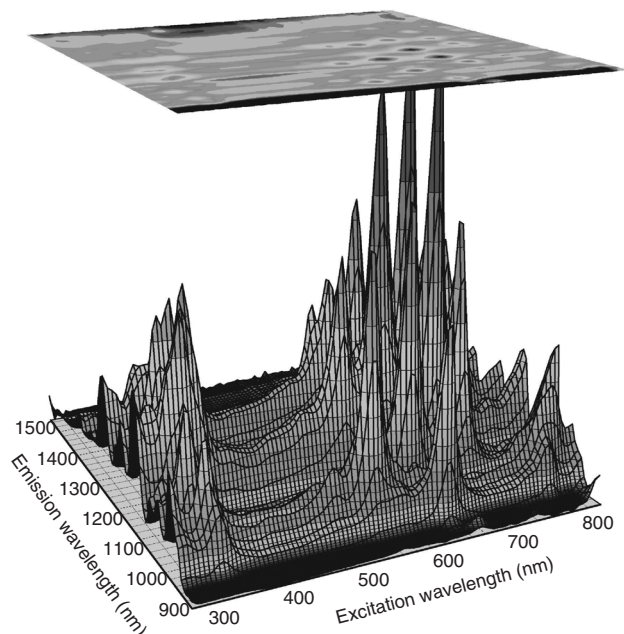
FIGURE 3.9 Fluorescence intensity vs. excitation and emission wavelengths for SWNTs in an SDS suspension.[67] Since each peak corresponds to the absorption/emission of a single (*n,m*) SWNT, the intensity of each peak provides a measure of the relative concentrations of each (*n,m*) SWNT in the sample.

The discrepancies obtained between various types of nanotube samples for the E_{22}^{S} and E_{11}^{S} transition energies (up to 100 meV) shows that the electronic energy levels that we use to distinguish one type of (*n,m*) SWNT from another is, in fact, sensitive to the different wrapping agents that are used, and to the different environments of the SWNTs (freely suspended, isolated SWNTs on various oxide substrates, in aqueous or organic solvents, etc.).[54] Such phenomena are currently under investigation.

3.2.6 FUTURE DIRECTIONS FOR NANOTUBE DEVELOPMENT

A large amount of information at the isolated SWNT level has provided accurate information about the structure and properties of single-wall carbon nanotubes and this has contributed in an important way to the development of more complete theoretical models to describe nanotube physics. Much effort must now be given to use these photophysics studies to characterize carbon nanotube systems in detail, because for such a nanometer scale system, the massless photon turns out to be a powerful probe for nanotube characterization without strongly disturbing this nanoscale system. For this reason we can expect spectroscopy to continue to provide an important tool for characterizing nanotube properties reliably.

Although sample purity can be investigated using the *D/G* band intensity ratio in the Raman spectra from SWNTs, the development of systematic work is needed

for quantitative information of sample purity using Raman spectroscopy. A quantitative procedure for the evaluation of the carbonaceous purity of bulk quantities of as prepared SWNT soot can be obtained by the utilization of solution-phase near-infrared spectroscopy.[68] However, for defect characterization at the single-nanotube level, development of the physics related to the defect-induced Raman *D*-band feature is needed. Such a development will be important for the characterization of more fancy nanotube-based devices, where any junction, kink, doping additive, or wrapping agent will be seen by the Raman effect as a defect, but will affect device performance differently. The challenge will be to see how each of these different types of defects can provide a different and distinguishable footprint in Raman spectroscopy. By using polarized light and exploiting selection rules at the single-nanotube level and by using near-field Raman spectroscopy, a variety of challenging and promising experiments can be carried out for the development of the next important phase of carbon nanotube photophysics characterization.

For applications of SWNTs as electronic devices it is essential to have a source of inexpensive, pure single-phase material, preferably with the same (*n,m*) indices. Although progress has been made in both the synthesis of a more uniform carbon nanotube product and in the separation of metallic from semiconducting nanotubes,[22] the current state of the synthesis technology is not sufficiently developed for large-scale nanotube electronics applications for commercial products. Development of (*n,m*) selective synthesis is the most challenging present goal for the development of carbon nanotube science and applications.

3.3 BISMUTH NANOWIRES

Nanowires are especially attractive for nanoscience studies as well as for nanotechnology applications. Nanowires, compared to other low-dimensional systems, have two quantum confined directions, while still leaving one unconfined direction for electrical conduction. This allows nanowires to be used in applications where electrical conduction, rather than tunneling transport, is required. Because of quantum confinement effects, nanowires in the limit of small diameters are expected to exhibit significantly different optical and electrical properties from their bulk 3-D crystalline counterparts and this is very much the case for bismuth nanowires. Their increased surface area, diameter-dependent band overlap and bandgap, and increased surface scattering for electrons and phonons are just some of the ways in which nanowires differ from their corresponding bulk materials, yet the diameters of typical bismuth nanowires are large enough (>5 nm) to have crystal structures closely related to their parent material, thereby allowing theoretical predictions about their properties to be made on the basis of an extensive literature relevant to bulk bismuth properties. Not only do bismuth nanowires exhibit many properties that are similar to, and others that are distinctly different from, those of their bulk counterparts, but they also have the advantage from an applications standpoint that some of their materials parameters that are critical for certain physical properties can be independently controlled in their nanowire form, but not in bulk bismuth, such as, for example, its thermal and electrical conductivity. Certain properties can also be enhanced non-linearly in small-diameter nanowires by exploiting the singular

aspects of the 1-D electronic density of states. Bismuth nanowires provide a promising framework for applying the bottom-up approach[69] for the design of nanostructures for nanoscience investigations and for potential nanotechnology applications as, for example, for thermoelectricity. It is the aim of this section to focus on bismuth nanowire properties that differ from those of bulk bismuth, with an eye toward possible applications that might emerge from the unique properties of these nanowires and from future discoveries in this field.

3.3.1 BISMUTH NANOWIRE SYNTHESIS

Bismuth (Bi) nanowires in principle can be prepared by many techniques[70] and it is expected that the synthesis of Bi nanowires by various novel techniques will become an even more active current research area than it has been. Most of the presently available physical property studies of bismuth nanowires have been made on nanowires grown in porous anodic alumina templates. A variety of other templates are available for use in growing bismuth nanowires, such as those prepared from nanochannel glass, diblock copolymers and ion track-etched polymer and mica films. Using porous anodic alumina templates (Fig. 3.10), highly crystalline bismuth nanowires with diameters in the 7–200 nm range and lengths up to 10 μm have been prepared with parallel alignment and a high packing density (~10^{11} nanowires/cm^2), which is favorable for a number of applications.[71] Nanochannel Vycor glass has been used to prepare Bi nanowires down to 4 nm diameter,[72] and the nanowires thus prepared have been useful for establishing the value of the wire diameter below which localization effects become important in electron transport, but the random organization of the pores, and consequently of the wires filling the template pores, would limit the range of applications of such nanowire arrays. Polymer-based templates might be desirable because of their favorable properties for certain applications (such as low thermal conductivity of the host material, which is desirable for thermoelectric applications), but because of their limitations for use at elevated
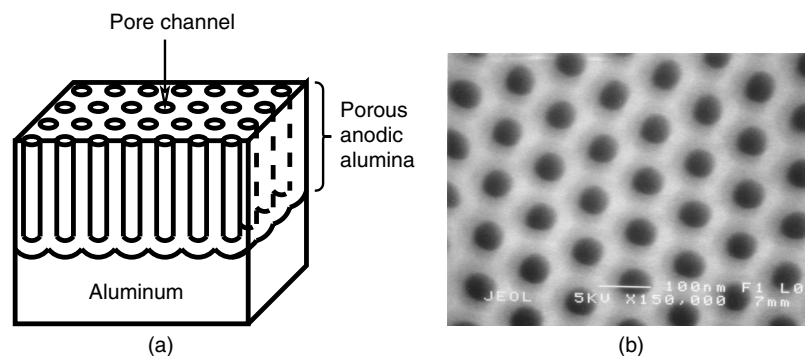

FIGURE 3.10 Porous anodic alumina templates showing (a) a schematic and (b) an SEM picture of the top surface.[75] The pores of these templates are filled to form nanowires.

temperatures, the filling of polymer-based templates would likely have to be done near room temperature by electrochemical means.[73,74]

The filling of the porous anodic alumina templates (Fig. 3.10) to form Bi nanowire arrays has been accomplished by at least three methods, including pressure injection, vapor growth, and electrochemical methods. Most of the properties measurements have been made with Bi nanowires prepared by pressure injection and vapor growth, though the electrochemical method is by far the most versatile and is the most logical candidate for scale-up for commercial applications.

The pressure injection technique can be employed for fabricating bismuth nanowires because of the low melting point of this material (271.4°C), though the porous template must be selected to have sufficient mechanical strength and stability to temperatures somewhat above the melting point of bismuth. In the high-pressure injection method, the nanowires are formed by pressure injecting the desired material in liquid form into the evacuated pores of the template. Due to the heating and the pressurization processes, the templates used for the pressure injection method must be chemically stable and be able to maintain their structural integrity at about 50 K above the melting point of bismuth at the injection pressure. Anodic aluminum oxide films and nanochannel glass are two typical host materials that have been used as templates in conjunction with the pressure injection filling technique.[76–78]

The pressure P required to overcome the surface tension for the liquid material to fill the pores with a diameter d_W is determined by the Washburn equation, $P = -4\gamma\cos\theta/d_W$, where γ is the surface tension of the liquid, and θ is the contact angle between the liquid and the template.[79] To reduce the required pressure and to maximize the filling factor, some surfactants are used to decrease the surface tension and the contact angle. For example, it is found that the introduction of a small amount of Cu in the Bi melt can facilitate the filling of the anodic alumina pores with liquid Bi and increase the number of nanowires that are prepared.[80] A typical pressure used for the preparation of bismuth nanowires is 0.3–1.5 kbar.[80,81] Nanowires produced by the pressure injection technique usually possess high crystallinity and a preferred crystal orientation along the wire axis.

The electrochemical deposition technique has attracted increasing attention as a promising alternative for fabricating nanowires because of its versatility and ability to produce bismuth nanowires of smaller diameter. Traditionally electrochemistry has been used to grow thin films on conducting surfaces. Since electrochemical growth is usually controllable in the direction normal to the substrate surface, this method can be readily extended to fabricate both quantum wire– and quantum dot–based nanostructures, if the deposition is confined within the pores of an appropriate template. In the electrochemical methods, a thin conducting metal film is first applied on one side of the porous membrane to serve as the working electrode for electroplating. The length of the deposited nanowires can be controlled by varying the duration of the electroplating process. This method has been used to synthesize a wide variety of electrically conducting nanowires including bismuth nanowires.[82]

In the electrochemical deposition process, the chosen template has to be chemically stable in the electrolyte during the electroplating process. Cracks and defects in the templates are detrimental to the nanowire growth, since electrochemical deposition processes will then primarily occur in the more accessible cracks, thus

leaving most of the nanopores unfilled. Particle track-etched mica films or polymer membranes are typical templates used in the simple DC electrolysis preparation method. To use anodic aluminum oxide films for DC electrochemical deposition, the insulating barrier layer that separates the pores from the bottom aluminum substrate has to be removed, and a metal film is then evaporated on to the back of the template membrane.[83] The electrochemical filling of anodic alumina templates has been carried out on both Bi and Bi_2Te_3.[84–86]

It is also possible to employ an AC electrodeposition method in filling anodic alumina templates without the removal of the barrier layer by utilizing the rectifying properties of the oxide barrier. In AC electrochemical deposition, although the applied voltage is sinusoidal and symmetric, the current is greater during the cathodic half-cycles, making deposition dominant over the etching, which occurs in the subsequent anodic half-cycles. Since no rectification occurs at defect sites, the deposition and etching rates are equal, and no material is deposited. Hence the difficulties associated with cracks are avoided. Pulse current electroplating techniques have been used for the synthesis of Bi nanowires[87,88] and they appear to be advantageous for the growth of crystalline wires generally because the metal ions in the solution can be regenerated between the electrical pulses and, therefore, more uniform deposition conditions can be produced for each deposition pulse.

One advantage of the electrochemical deposition technique is the possibility of fabricating multilayered structures within nanowires. By varying the cathodic potentials in the electrolyte, which contains two different kinds of ions, layers of different compositions can be controllably deposited. This electrodeposition method provides a low-cost approach to prepare multilayered 1-D nanostructures. One disadvantage of the electrochemical deposition approach for applications is that the Bi nanowires fabricated by the electrochemical process are often polycrystalline, with no preferred crystal orientations. Progress has been made in improving the crystallinity of Bi nanowires prepared by the electrochemical route by careful control of the deposition parameters.[75,89–91]

Vapor deposition is a convenient method for filling the template pores with bismuth and is usually capable of preparing smaller diameter ($\leq$20 nm) nanowires than pressure injection methods, since it does not rely on high pressure to overcome the surface tension involved in inserting the bismuth into the pores of the template. In the physical vapor deposition technique, the bismuth is first heated to produce a vapor, which is then introduced through the pores of the template, and the template is subsequently cooled to solidify the bismuth nanowires. Using a specially designed experimental setup,[92] nearly single-crystal Bi nanowires in anodic aluminum templates with pore diameters as small as 7 nm have been synthesized, and these Bi nanowires were found to possess a preferred crystal growth orientation along the wire axis, similar to the Bi nanowires prepared by pressure injection.[92]

Once the bismuth nanowires are grown in a template, it is possible to etch away the template in appropriate acids to gain access to the individual nanowires. An example of a sample of such free-standing bismuth nanowires on a silicon substrate is shown in Fig. 3.11.

Although porous alumina templates provide a convenient method for preparing arrays of nanowires for study and demonstration purposes, these arrays have some
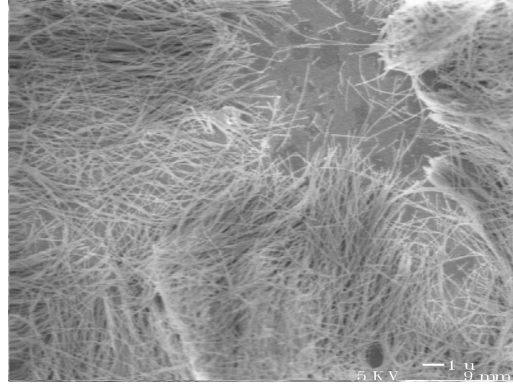
FIGURE 3.11 Bismuth nanowires on a silicon wafer exposed by etching the porous anodic alumina film.

severe disadvantages for large scale applications. Porous anodic alumina is a brittle ceramic film grown on a soft aluminum metal substrate. Great care needs to be exercised in the preparation of the aluminum substrate and in the manipulation of the anodic film to produce pure defect-free porous anodic alumina films, which are required in order to achieve uniform filling of the pores with the nanowire material. Moreover between the porous layer and the aluminum substrate, there is a continuous and dense alumina barrier layer that prevents the direct physical and electrical contact between the pore (or nanowire) and the substrate. It is therefore of great interest to develop methods to grow porous anodic alumina films on rigid substrates of technological relevance and to establish contact to both ends of the pores (or of the nanowires) while the film is still attached to the substrate. Such technology would allow one to integrate addressable arrays of parallel nanowires as active components in electronic, thermoelectric, optical, field emission, and sensing devices.

Techniques have recently been developed to grow arrays of bismuth nanowires on the surface of a silicon wafer coated with a porous anodic alumina film.[93] A conducting layer under the porous film serves as the working electrode for the electrochemical growth of the nanowires array. An example of bismuth nanowires electrochemically grown on the surface of a silicon wafer is shown in Fig. 3.12.[75,93] Unlike free standing porous alumina films containing bismuth nanowires, the films grown on a silicon wafer are robust enough to allow growth on large areas of the silicon wafer. Furthermore, patterned porous films and patterned electrodes can be used to control the location and the shape of the nanowire array using conventional microelectronics fabrication techniques.

3.3.2 STRUCTURAL CHARACTERIZATION

Thus far most of the emphasis on the structural characterization of bismuth nanowires has been in terms of their degree of crystallinity and the crystalline orientation of the nanowire axis. The reason for this focus on crystallinity stems from the
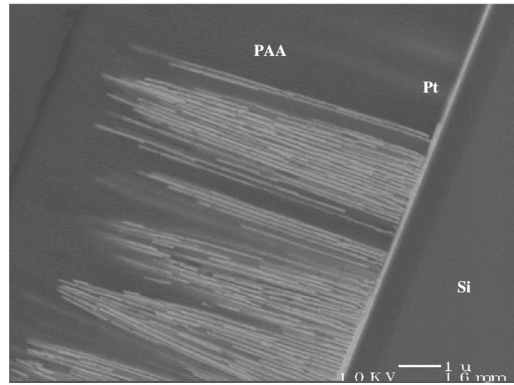
FIGURE 3.12 Cross section of an array of bismuth nanowires grown on a platinum (Pt) coated silicon (Si) wafer, allowing more robust growth of bismuth nanowires in porous anodic alumina (PAA) films over large areas on a silicon wafer.[93]

extraordinarily large anisotropy of the effective mass components and consequently of the constant electronic energy surfaces of crystalline bismuth.[71] This anisotropy is responsible for the exceptional electronic properties of bismuth and for the interest in bismuth nanowires both as a model system for studying 1-D physics phenomena and for possible future practical applications.

Scanning electron microscopy (SEM) produces images of bismuth nanowires down to length scales of ~10 nm, and provides valuable information regarding the structural arrangement, the spatial distribution of the nanowires, the filling factor of the nanowires in space, the morphological features of individual nanowires, and arrays of nanowires. Since many of the studies of bismuth nanowires have been made on arrays of bismuth nanowires in templates, SEM has also provided valuable characterization of the templates used to grow the nanowires to determine the pore diameters and diameter distribution in the template arrays, the packing fraction, and the filling factor, as illustrated in Fig. 3.10, where the top view of a typical empty anodic alumina template is shown. After the template has been filled with bismuth (by either liquid phase pressure injection, vapor phase injection, or electrochemical filling), the filling factor can be determined utilizing the very high contrast of the secondary electron emission (electron absorption) of the bismuth nanowire as compared to the very low interaction of the electron probes with the empty pores of the template.

Transmission electron microscopy provides a wide range of characterization information about bismuth nanowires including their crystal structure, crystal quality, grain size, and crystalline orientation of the nanowire axis. When operating in the diffraction mode, selected-area electron diffraction (SAED) patterns can be taken to determine the crystal structure of nanowires. The amount of crystallinity of individual nanowires is evaluated from lattice fringe images, such as the one shown in Fig. 3.13(a). Here we can see from the regularity of the lattice fringes that pressure injection produces bismuth nanowires with a high degree of crystallinity. The crystalline quality of bismuth nanowires obtained by vapor phase growth is also very high.
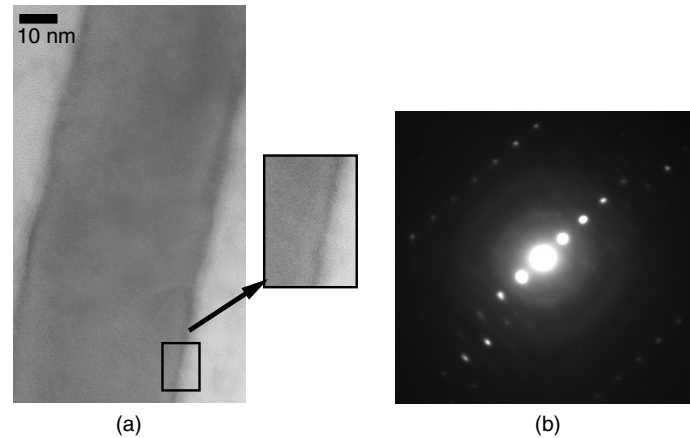
FIGURE 3.13 (a) HRTEM image of a free-standing individual Bi nanowire with a diameter of 45 nm. The inset, shown in an enlarged form on the right, highlights the lattice fringes of the nanowire, indicating high crystallinity. (b) Selected-area electron diffraction (SAED) pattern of the same nanowire in the TEM image.[94]

To establish the crystalline direction of the nanowire axis, SAED measurements are made at the individual nanowire level (Fig. 3.13(b)). Such SAED patterns can also be used to establish the degree of crystallinity along a single nanowire by taking multiple SAED spectra at different points along the nanowire axis, and SAED measurement of several nanowires gives information about the distribution of the crystalline orientations.

X-ray diffraction (XRD) measurements on an array of aligned bismuth nanowires inside their templates can be used to get information about the crystallographic orientation of the nanowires within a single template, as shown in Fig. 3.14. What is seen here is a high degree of crystallinity with >80% crystalline orientation of the nanowire along a specific nanowire direction. The large diameter (>95 nm) nanowires show a nanowire alignment predominately along a (101) axis, while the smaller diameter nanowires ($\leq$40 nm) show predominant alignment along an (012) axis, suggesting a wire diameter–dependent crystal growth mechanism. On the other hand, 30-nm Bi nanowires produced using a much higher pressure of >1.5 kbar show a different crystal orientation of (001) along the wire axis,[81] indicating that the preferred crystal orientation may also depend on the applied pressure, with the most dense packing direction along the wire axis for the highest applied pressure. The crystallinity and orientation of vapor-grown bismuth nanowires in the alumina templates are similar to those prepared by pressure injection. Although early work on the electrochemical preparation of Bi nanowires produced less crystalline nanowires than the vapor-grown or pressure injection methods, subsequent efforts[89–91] have produced aligned- and single-crystal nanowires, with crystal orientations along the wire axes depending on the preparation conditions. X-ray energy dispersion analysis also provides information on the impurity content of the bismuth nanowires. XRD and
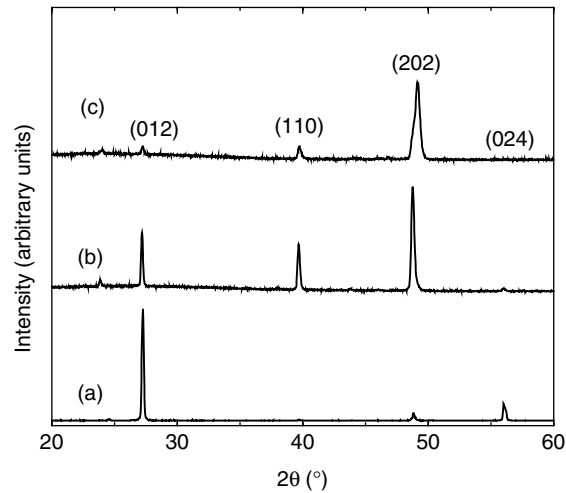
FIGURE 3.14 XRD patterns of bismuth/anodic alumina nanocomposites with average bismuth wire diameters of (a) 40 nm, (b) 52 nm, and (c) 95 nm.[78] The Miller indices corresponding to the lattice planes of bulk Bi are indicated above the individual peaks. The majority of the Bi nanowires are oriented along the $[10\bar{1}1]$ and $[01\bar{1}2]$ directions for $d_W \geq$ 60 nm and $d_W \leq 50$ nm, respectively.[78] The existence of more than one dominant orientation in the 52-nm Bi nanowires is attributed to the transitional behavior of intermediate-diameter nanowires as the preferential growth orientation is shifted from $[10\bar{1}1]$ to $[01\bar{1}2]$ with decreasing d_W.

TEM characterization of $Bi_{1-x}Sb_x$ alloy nanowires for $x \leq 0.15$ prepared by the pressure injection method[94] show good compositional homogeneity along the nanowire axis, good crystallinity of the alloy nanowires, with the same preferred crystalline alignment of the nanowire axis, as is the case of pure bismuth nanowires. On the other hand, a gradient in alloy composition along the nanowire axis was determined by EDAX in 200-nm Sb-rich $Bi_{1-x}Sb_x$ nanowires electrochemically deposited in porous alumina templates.[75] It is significant that the SAED patterns (such as in Fig. 3.13(b)) taken on individual nanowires by electron diffraction are in good agreement with the x-ray diffraction patterns taken on large arrays of nanowires, as in Fig. 3.14.

The high resolution of the TEM also allows for the investigation of the surface-structure of bismuth nanowires, which form native surface oxides when exposed to oxidative conditions (i.e., atmospheric air). Knowledge of the surface composition and structure are very important for transport applications of bismuth and related nanowires, as, for example, for thermoelectric cooling or thermal management applications.[71] In an attempt to control the formation of these oxide surface layers, the surface structure of bismuth nanowires has been studied by using an *in situ* environmental TEM chamber, which allows TEM observations to be made while different gases are introduced or as the sample is heat treated at various temperatures, as illustrated in Fig. 3.15. This figure shows the high resolution TEM images of a Bi nanowire with an oxide coating and the
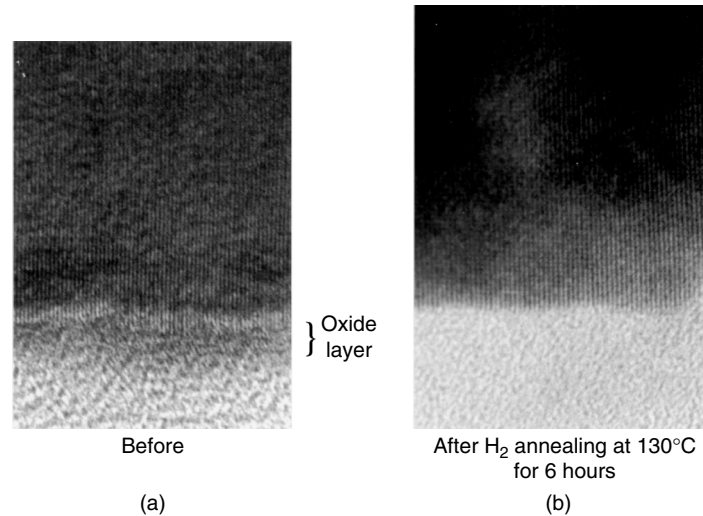
Before

(a)

After H$_2$ annealing at 130°C
for 6 hours

(b)

Oxide layer

FIGURE 3.15 High-resolution transmission electron microscope (HRTEM) image of a Bi nanowire (a) before and (b) after annealing in hydrogen gas at 130°C for 6 hours within the environmental chamber of the HRTEM instrument to remove the oxide surface layer.[95]

effect of a dynamic oxide removal process carried out within the environmental chamber of the TEM.[95] The amorphous bismuth-oxide layer coating of the nanowire (Fig. 3.15(a)) is removed by exposure of the wire to hydrogen gas within the environmental chamber of the TEM, as indicated in Fig. 3.15(b).

By coupling the powerful imaging capabilities of TEM with other characterization tools, such as an electron energy loss spectrometer (EELS) or an energy dispersive X-ray spectrometer (EDS) within the TEM instrument, additional properties of the nanowires can be probed with high spatial resolution. With the EELS technique, the energy and momentum of the incident and scattered electrons are measured in an inelastic electron scattering process to provide information on the energy and momentum of the excitations in the nanowire sample. Figure 3.16 shows the dependence on nanowire diameter of the electron energy loss spectra of Bi nanowires.[96] The spectra were taken from the center of the nanowire, and the shift in the energy of the peak position (Fig. 3.16) is used to monitor the plasmon frequency in the bismuth nanowires as the nanowire diameter is varied. The results show that there are changes in the electronic structure of Bi nanowires as the wire diameter decreases. Such changes in electronic structure as a function of nanowire diameter are related to quantum confinement effects, which are also observed in their transport and optical properties, as discussed in the next section.

3.3.3 ELECTRONIC CHARACTERIZATION

Bismuth in bulk form is a semimetal, and therefore when undoped, bulk bismuth has an equal number of electrons and holes, each with highly anisotropic constant energy surfaces. The corresponding highly anisotropic Fermi surfaces make bismuth
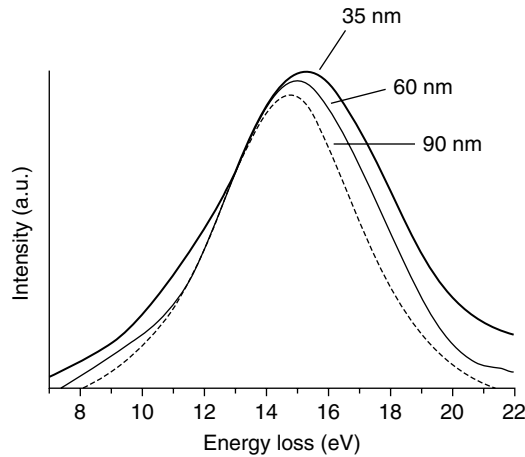
FIGURE 3.16 Electron energy loss spectra (EELS) taken from the center of bismuth nanowires with diameters of 35, 60, and 90 nm. The shift in the volume plasmon peaks is due to the wire diameter effects on the electronic structure.[96]

very interesting from an applications standpoint, because it is this aspect of bismuth that makes the electronic properties of bismuth nanowires so different from bulk bismuth. Because of the very small effective mass components of bismuth, the subbands that are formed under quantum confined conditions are widely spaced in energy. Thus, as the nanowire diameter decreases, the lowest conduction subband increases in energy, while the highest valence subband decreases in energy, thereby decreasing the band overlap between the valence and conduction band, which is 38 meV for bulk bismuth and for Bi nanowires of very large diameter (Fig. 3.17). The figure further shows that at a nanowire diameter of about 50 nm the band overlap at 77 K goes to zero and bismuth nanowires become semiconducting. As the nanowire diameter further decreases, the bandgap of the semiconducting nanowires increases, as is also seen in Fig. 3.17. The figure also shows that the diameter where the semimetal-semiconductor transition occurs is dependent on the crystalline orientation of the nanowire along its axis, with the transition occurring at the largest diameter (55 nm) for wires oriented along the highest symmetry direction, which is the three-fold trigonal symmetry direction.

What is exceptional about bismuth is that because of the highly anisotropic constant energy surfaces, the effective mass components normal to the light mass component can be quite heavy. This means that it is possible to achieve very high carrier mobility along the nanowire axis by having conduction along a high-mobility, low effective-mass crystallographic direction, while at the same time having a reasonably high density of states, associated with the heavy carrier masses. Such an unusual situation is very beneficial for such applications as thermoelectricity.

It would seem that the best way to study these anisotropic properties would be through measurements of the temperature dependence of the resistivity of individual bismuth nanowires. However, the incorporation of bismuth nanowires into test device
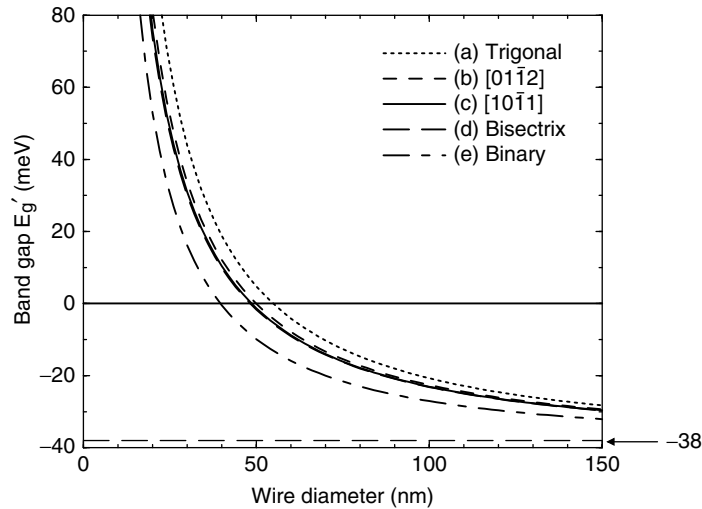
FIGURE 3.17 Calculated bandgap energy between the lowest electron subband and the highest hole subband of Bi nanowires oriented along the (a) trigonal, (b) [01$\bar{1}$2], (c) [01$\bar{1}$1], (d) bisectrix, and (e) binary crystallographic directions as a function of wire diameter. The nonparabolic effects of the L-point electron pockets have been taken into account, and cylindrical wire boundary conditions are used in the calculations. The values of d_c, the critical wire diameter, where the semimetal-to-semiconductor transition occurs, are 55.1, 50.0, 49.0, 48.5, and 39.8 nm for nanowires oriented along the trigonal, [01$\bar{1}$2], [01$\bar{1}$1], bisectrix, and binary directions, respectively. The curves for the bisectrix and [01$\bar{1}$1] directions are too close to one another to be resolved.[94]

structures for such measurements has not yet been explored extensively. Two- and four-point resistance test structures have been prepared (see Fig. 3.18) by photolithography (or e-beam lithography), and metal deposition of contacts has been done on individual bismuth nanowires dispersed on an oxidized silicon wafer substrate.[97,98] The challenge in studying the temperature dependence of individual bismuth nanowires has been the fabrication of reliable contacts to these nanowires, because of the native oxide coating that forms on their surfaces. Progress thus far has been made in developing reliable ohmic contacts that are stable over the 2–400 K temperature range. A method for avoiding the burnout of bismuth nanowires due to electrostatic discharge has also been developed.[97]

The experimental verification of the transition from semimetallic bulk bismuth to a semiconducting nanowire can be observed in transport measurements of the temperature-dependent resistance of nanowire array, as shown in Fig. 3.19(a). Here the temperature-dependent resistance is normalized to its value at 300 K because the number of nanowires in the template to which electrical contact is made is not known. Figure 3.19(a) shows that the temperature-dependent normalized resistance $R(T)/R(300\ K)$ changes radically from the curve for the bulk sample to that for a 200 nm diameter nanowire sample, where a peak in the normalized
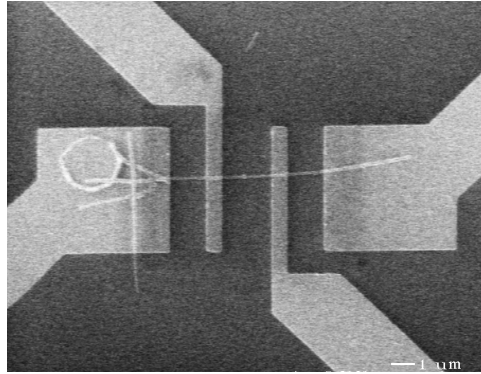
FIGURE 3.18 SEM image of four contacts to a single bismuth nanowire used for transport measurements.[98]

$R(T)/R$(300 K) curve appears. The peak gains prominence as fewer and fewer subbands contribute to the carrier conduction, as shown by the experimental results for the 70 nm diameter nanowire. This behavior is further confirmed by a model calculation of the normalized resistance $R(T)/R$(300 K) (Fig. 3.19(b)). Finally when the wire diameter enters into the semiconductor regime below 50 nm (Fig. 3.17), the experimental
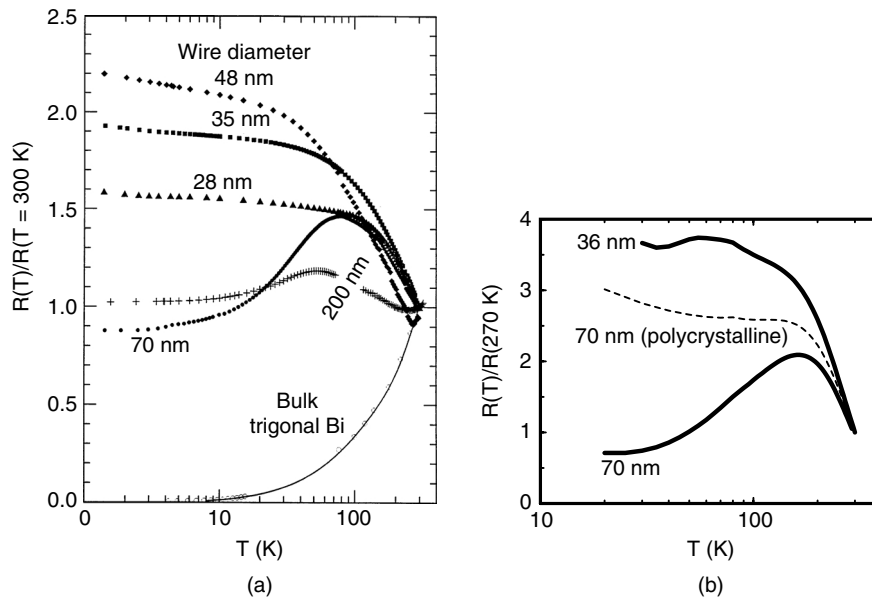
FIGURE 3.19 (a) Measured T dependence of the normalized resistance $R(T)/R$(300 K) for highly crystalline Bi nanowires of various d_w.[92] (b) Calculated $R(T)/R$(300 K) for 36- and 70-nm Bi nanowires.[78] The dashed curve refers to a 70-nm polycrystalline wire with increased grain-boundary scattering.

curves for $R(T)/R(300\ K)$ in Fig. 3.19(a) show a different monotonic functional form, as seen by comparing the experimental curves in this lower diameter range with results shown for wire diameters of 200 nm and 70 nm.[92] Model calculations for nanowires in the semiconducting regime (Fig. 3.19(b)) reproduce the observed form of $R(T)/R(300\ K)$.[78] To further verify the validity of the model calculations, a curve for $R(T)/R(300\ K)$ for polycrystalline bismuth wires was calculated (Fig. 3.19(b)) and these results are also in good agreement with measurements of Hong et al.[99]

Further evidence for the semimetal-semiconductor transition in bismuth nanowires comes from measurements made on randomly oriented bismuth nanowires of very small diameter prepared in the pores of silica, Vycor glass, and alumina templates.[72] The wire diameters in this case were sufficiently small so that the bandgaps were large enough to get large resistance changes of several orders of magnitude over the measured temperature range, so that a fitting of the experimental points could be made to the functional form $R(T) = R_0\exp(-E_g/kT)$, as shown in Fig. 3.20(a), in order to obtain a measure of the bandgap. The results thus obtained for the semiconducting bandgap are shown in Fig. 3.20(b),[72] and good agreement is obtained for these experimental results with theoretical predictions[100] for the

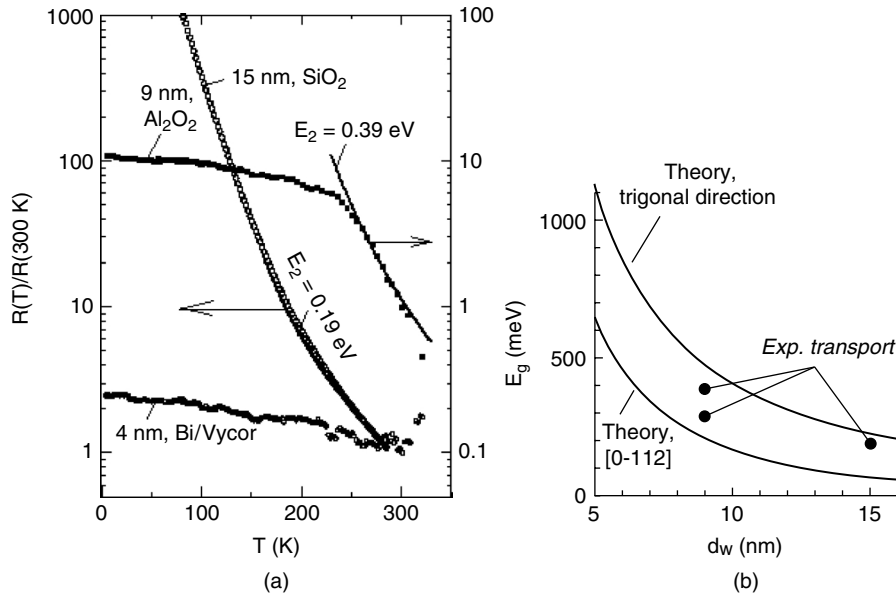**FIGURE 3.20** (a) Temperature dependence of the normalized resistance $R(T)/R(300\ K)$ for Bi nanowires for randomly oriented nanowires with various diameters in the range $d_w \leq 15$ nm in silica, alumina, and Vycor glass templates, as indicated in the figure. The points are experimental data, while the lines are fits to $R(T) = R_0\exp(-E_g/kT)$.[72] (b) Calculated[100] values for the energy gap of Bi nanowires as a function of wire diameter d_w for two different crystallographic orientations of the nanowire axis (Fig. 3.17). The points are the experimental values of E_g obtained from fits to $R(T) = R_0\exp(-E_g/kT)$ fitted to three different samples as shown in (a).[72]

temperature dependence of the semiconducting bandgap. Using these very thin bismuth nanowires allowed exploration for carrier localization effects at low temperature.[75]

The semimetal-semiconductor transition in nanowires can also be probed by examination of the effect of doping. In the case of bismuth nanowires, doping with isoelectronic antimony allows variation of the nanowire diameter at which the semimetal-to-semiconductor phase transition occurs. As a 3-D system, $Bi_{1-x}Sb_x$ alloys form a substitutional 3-D solid-state system over the entire range of compositions x. As shown in Fig. 3.21(a) the band overlap of bismuth decreases upon Sb addition and the alloys become semiconductors for x in the range $0.07 < x < 0.22$ with a bandgap that depends on x. For $0.09 < x < 0.16$, Fig. 3.21(a) shows that the $Bi_{1-x}Sb_x$ bulk alloy is a direct gap semiconductor, with both electron and hole pockets located at the L points in the Brillouin zone (see inset of Fig. 3.21(b)). In the range $0.07 < x < 0.09$, the $Bi_{1-x}Sb_x$ bulk alloy is an indirect gap semiconductor with a hole pocket at the T point, while in the range $0.16 < x < 0.22$, the alloy is an indirect gap semiconductor with holes forming around the six H-points shown in the inset of Fig. 3.21(b). Therefore by antimony addition, the electronic band structure of $Bi_{1-x}Sb_x$ can be modified over a wide range of electronic behaviors, suggesting that $Bi_{1-x}Sb_x$ alloy nanowires should constitute an interesting 1-D system in which the electronic band structure and related properties can be varied over an even wider range of behaviors than for 3-D $Bi_{1-x}Sb_x$ by combining the quantum confinement effect with the Sb alloying effect.

Figure 3.21(b) displays the phase diagram of $Bi_{1-x}Sb_x$ nanowires as a function of wire diameter and Sb concentration.[101] This phase diagram is calculated[101] assuming the same unit cell geometry as occurs in the parent bulk $Bi_{1-x}Sb_x$ alloy, consistent with x-ray diffraction measurements. As can be seen from Fig. 3.21(b), there are two regions where a semimetal-to-semiconductor phase transition occurs, one involving L-point electrons and T-point holes (upper left of Fig. 3.21(b)), out to nearly $x = 0.05$ for a 100-nm nanowire, and the second region involving L-point electrons and H-point holes (upper right of Fig. 3.21(b)), extending to $x = 0.24$ for a 100-nm nanowire, but providing a semiconducting phase for small-diameter wires over a much larger Sb concentration range than in the bulk alloy.[101] The inset in Fig. 3.21(b) shows the Brillouin zone of the $Bi_{1-x}Sb_x$ alloy system and the locations of the L, H, and T points in the rhombohedral Brillouin zone. The semimetal-to-semiconductor phase transition involving the T-point holes and the L-point electrons, as indicated by the phase boundary line in Fig. 3.21(b), have been probed experimentally by temperature-dependent normalized resistance measurements, as discussed subsequently. The critical wire diameter d_c for the semimetal-to-semiconductor transition is about 50 nm for pure bismuth nanowires at 77 K, but d_c increases with increasing Sb concentration for $Bi_{1-x}Sb_x$ alloy nanowires. We note from Fig. 3.21(b) that the x range of the semiconducting phase for $Bi_{1-x}Sb_x$ nanowires broadens as the wire diameter decreases.

The semimetal-to-semiconductor phase transition was determined in the $Bi_{1-x}Sb_x$ nanowire system by measurement of the normalized temperature-dependent resistance $R(T)/R(270\ K)$ for 65 nm diameter nanowires of different Sb alloy composition x, as shown in Fig. 3.22. In this figure the measured normalized resistance of pure bismuth shows a non-monotonic T dependence with a maximum at ~70 K,
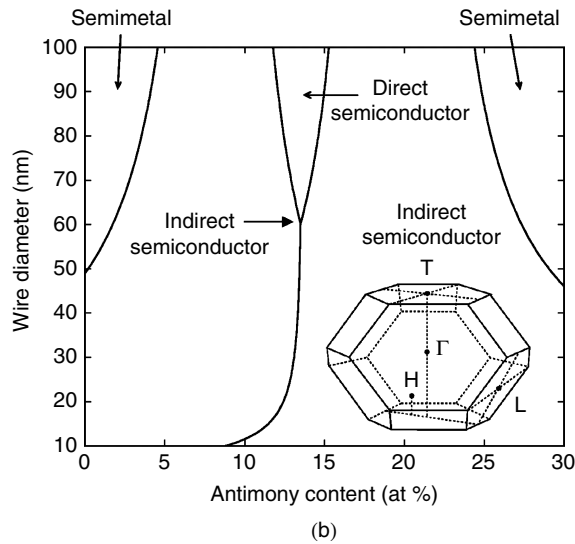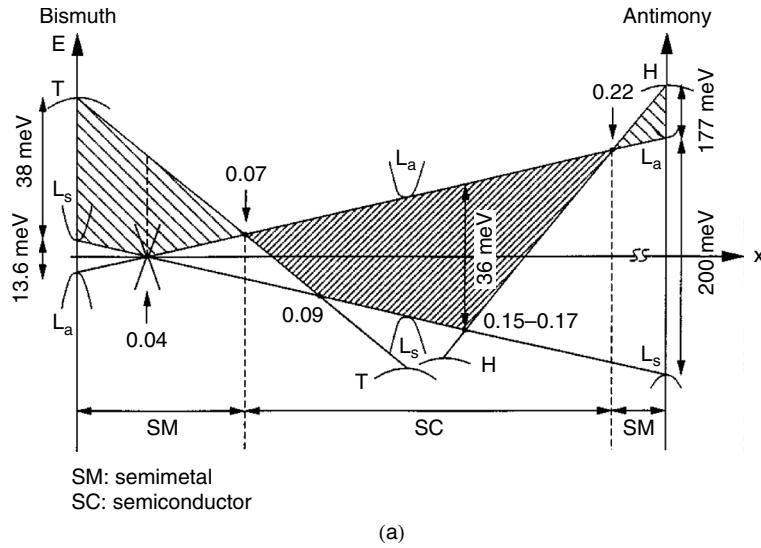
(a)

(b)

FIGURE 3.21 Diagrams for the electronic phases for (a) 3-D bulk $Bi_{1-x}Sb_x$ plotted as energy vs. composition[75] and for (b) $Bi_{1-x}Sb_x$ nanowires as a function of wire diameter and Sb concentration.[101]

while the resistivities of the alloy nanowire samples (with 5 at.% and 10 at.% Sb) decrease monotonically with increasing *T*, characteristic of the semiconducting phase (Fig. 3.19(a)). Furthermore, $R(T)/R(270\ K)$ for the $Bi_{0.95}Sb_{0.05}$ nanowires display a stronger *T* dependence than that of the $Bi_{0.90}Sb_{0.10}$ nanowires. The saturation of $R(T)/R(270\ K)$ at low *T* for all the three nanowire compositions is attributed to carriers associated with uncontrolled impurities that are estimated to
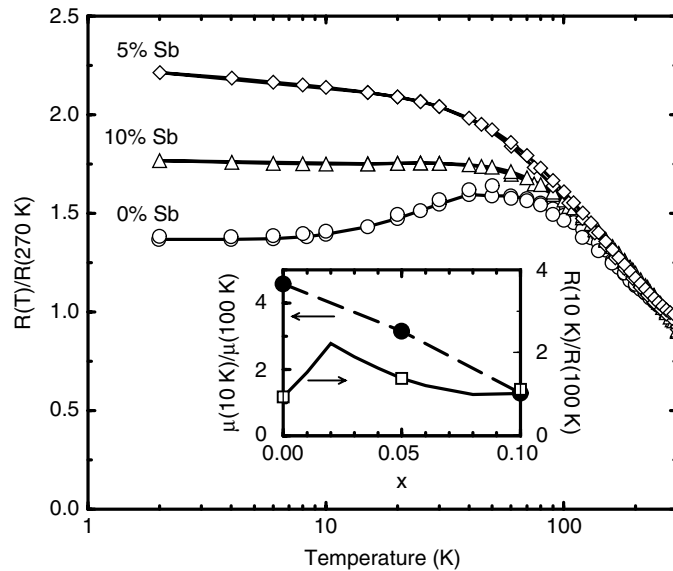
FIGURE 3.22 Measured temperature dependence of the 270 K normalized resistance of 65-nm $Bi_{1-x}Sb_x$ nanowires with different Sb contents. The inset shows ratios of the mobility $\mu(10\text{ K})/\mu(100\text{ K})$ between 10 K and 100 K for the three samples (•) and the ratios of the resistance $R(10\text{ K})/R(100\text{ K})$ (□) as a function of Sb content, where the points are experimental values and the curves are predictions.[102]

have a concentration of about $1 - 4 \times 10^{16}/\text{cm}^3$. The carriers associated with the uncontrolled impurities become increasingly important as the bandgap of the semiconductor increases (Fig. 3.17). Based on the calculated temperature-dependent carrier concentration and the measured normalized temperature-dependent resistance $R(T)/R(270\text{ K})$ shown in Fig. 3.22, the temperature-dependent average mobility ratio $\mu(T)/\mu(100\text{ K})$ is obtained for the three samples in Fig. 3.22. These calculations are then used to predict the Sb concentration at which the semimetal to semiconductor transition occurs, as indicated in Fig. 3.22, and the result is found to be in very good agreement with the theoretical prediction for this transition at $x \simeq 0.02$ for a 65-nm $Bi_{1-x}Sb_x$ nanowire, as shown in Fig. 3.21(b). Confirmation of the phase diagram shown in Fig. 3.21(b) allows this diagram to be used for guidance in designing nanowires in the semiconducting phase with some control of the bandgap of semiconducting bismuth as well as some control of other nanowire properties.

Measurements of the temperature-dependent Seebeck effect using the smallest available thermocouples for temperature sensors, as shown in Fig. 3.23(a), provide further support for the phase diagram shown in Fig. 3.23(b). The data in Fig. 3.23(b) show an increase in the magnitude of the Seebeck coefficient either as the wire diameter of bismuth nanowires decreases, or as Sb is added to form a $Bi_{1-x}Sb_x$ alloy. Further enhancement of the magnitude of the Seebeck coefficient is achieved when both the nanowire diameter decreases and Sb is added, as shown in Fig. 3.23(b).[102,103]
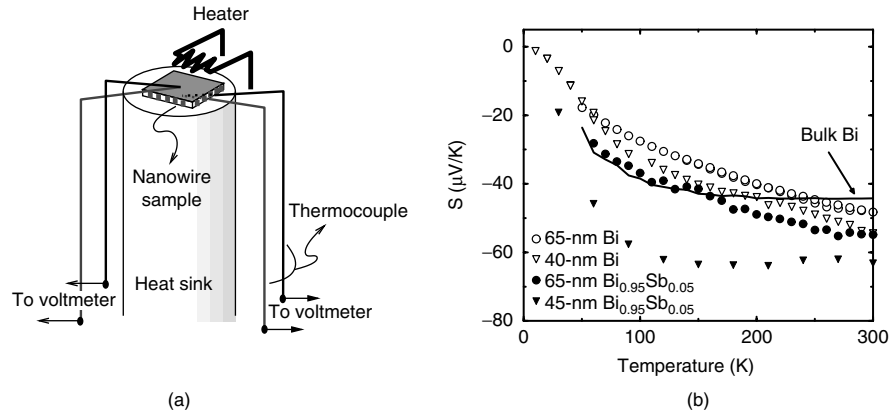
FIGURE 3.23 (a) Experimental setup of Seebeck coefficient measurement for nanowire arrays. (b) Measured Seebeck coefficient as a function of T for Bi and $Bi_{0.95}Sb_{0.05}$ nanowires with different diameters. The solid curve denotes the Seebeck coefficient for bulk Bi.[102]

3.3.4 OPTICAL CHARACTERIZATION

Even though the bismuth nanowire diameter is typically an order of magnitude smaller than the wavelength of light, optical reflectivity and transmission measurements have nevertheless been used successfully to characterize bismuth nanowires.[104,105] What is surprising is that the intense and sharp absorption peak that dominates the infrared absorption spectrum in bismuth nanowires,[104,105] is not observed in bulk bismuth. The energy position E_p of this strong absorption peak increases with decreasing diameter. However, the rate of increase in energy with decreasing diameter $|\partial E_p/\partial d_W|$ is an order of magnitude less than that predicted for either a direct interband transition or for intersubband transitions in bismuth nanowires. On the other hand, the magnitude of $|\partial E_p/\partial d_W|$ agrees well with that predicted for an indirect L-point valence to T-point valence band transition (see insets to Fig. 3.21(b)). Since both the initial and final states for the indirect L-T point valence band transition downshift in energy as the wire diameter d_W is decreased, the shift in the absorption peak results from a *difference* between the effective masses for these two carrier pockets and is less sensitive to the actual value of either of the masses. Hence the diameter dependence of the absorption peak energy is an order of magnitude less for a valence-to-valence band indirect transition than for a direct interband L-point transition. Furthermore the band-tracking effect for this indirect transition gives rise to a large value for the joint density of states, thus accounting for the high intensity of this feature. This indirect transition arises through the gradient of the dielectric function, which is large at the bismuth-air or bismuth-alumina interfaces. In addition, the intensity can be quite significant because there are abundant initial state electrons, final state holes, and appropriate phonons are available for making an indirect L-T point valence band transition at room temperature. Interestingly the polarization dependence of this absorption peak is such that the strong absorption is present when the electric field is perpendicular to the wire axis, but is absent when the electric

field is parallel to the wire axis, contrary to a traditional polarizer, such as a carbon nanotube where the optical *E* field is polarized by the nanotube itself to be aligned along the carbon nanotube axis. The observed polarization dependence for bismuth nanowires is consistent with a surface-induced effect that increases the coupling between the *L*-point and *T*-point bands throughout the full volume of the nanowire. The indirect *L* to *T* point valence band transition mechanism[104,105] is also consistent with observations of the effect on the optical spectra of a decrease in the nanowire diameter and of *n*-type doping of bismuth nanowires with Te.[104]

3.3.5 FUTURE DIRECTIONS FOR BISMUTH NANOWIRES

Bismuth nanowires are likely to provide a model system for future nanowire studies because of their unique properties, namely their highly anisotropic constant energy surfaces, which allow these nanowires to simultaneously have high mobility carriers at a reasonable high electronic density of states and to exhibit quantum effects at relatively high nanowire diameter. The anisotropy associated with the nanowire geometric structure breaks the symmetry so that the wire axis can be chosen to be along a low effective mass/high carrier mobility direction simultaneously. In this way, the highly anisotropic constant energy contours of bismuth can be explicitly exploited to yield the quantum confinement of the carriers that is responsible for the various semimetal-to-semiconductor electronic phase transitions. This phase transition allows the special electronic properties to be utilized in a semiconducting form of pure bismuth and over an extended range of wire diameter and of chemical composition in $Bi_{1-x}Sb_x$ alloy nanowires. Using the same dopants as are used in bulk bismuth to add electrons (from column IV in the periodic table) and to add holes (from column VI), semiconducting devices based on this nanowire system should be possible, as, for example, for thermoelectric applications.

Future progress in this field will be significantly enhanced by developing better bismuth nanowire synthesis methods yielding nanowires that are highly crystalline (so that the anisotropic electronic energy band structure can be exploited) and to which good electrical contacts can be made (circumventing the problems caused by surface oxidation when Bi nanowires are exposed to ambient conditions). If templates are used for nanowire self-assembly, electrical isolation and crystallographic alignment of nanowire arrays, more rugged template materials are needed, and for thermoelectric applications, template materials with lower thermal conductivity would be needed. The ability to control nanowire materials properties that are linked together in bulk bismuth but are not so closely linked in bismuth nanowires requires further exploration through model-based selection of wire diameter and $Bi_{1-x}Sb_x$ alloy composition.

3.3.6 CONCLUDING REMARKS

When considering the one-dimensionality of bismuth, some comment is in order about the ability of bismuth (and many other materials systems for that matter) to form nanotubes as well as nanowires by a variety of synthesis approaches, including growth in templates initiated at the pore interfaces and using very short growth times.[106]

One interesting aspect of a bismuth nanotube is that the wall thickness can be a single basic structural unit consisting of two atomic layers. The diffraction pattern for bismuth nanotubes reveals lattice constants similar to those of 3-D bismuth. Research on the physical properties of bismuth nanotubes is at an early stage, and the electronic structure remains to be explored. Study of the electronic structure of bismuth nanotubes in relation to that of bismuth nanowires with a similar local atomic arrangement and a similar outer diameter should prove to be fascinating. Also intriguing should be the comparison of the electronic structure of a bismuth nanotube to that of a carbon nanotube. Although bismuth and graphite are both semimetals as 3-D crystals, their electronic structures as 1-D nanowires and nanotubes, respectively, are quite different, and it is expected that the electronic structure of a bismuth nanotube will differ significantly from its nanowire counterpart, as well as from that of a carbon nanotube.

From these considerations we can conclude that we are now within reach of studying the rich variety of electronic structures that 1-D systems might exhibit, how to realize this variety of structures experimentally, and eventually how to exploit these different electronic structures to yield interesting materials properties not yet achieved in any system, and how perhaps to utilize these special properties someday for practical applications.

ACKNOWLEDGMENTS

PROBLEMS

1. Based on the cutting lines concept, explain why for an (n,m) single-wall carbon nanotube (SWNT) the nanotube is a large bandgap semiconductor, when $n - m$ is not a multiple of three, with the band gap increasing as the diameter decreases ($1/d_t$ dependence), while the nanotube shows metallic behavior (at room temperature) for $n - m = 3j$ (j = integer). Compare the electronic density of states near the Fermi level for semiconducting and metallic SWNTs and for a 2-D graphene sheet.

2. How are single-wall carbon nanotubes formed in the laboratory? Which mechanism for SWNT growth (catalytic root growth or tip growth) is most probable for the synthesis of very long (~cm) tubes? What are the major challenges that need to be addressed in advancing carbon nanotube synthesis?

3. List the common methods for nanotube characterization, and their advantages and limitations. What is it that each characterization method probes and why is it important to gain this information?

4. Why is Raman spectroscopy a particularly valuable tool for the study and characterization of carbon nanotube systems? What are its advantages and limitations?
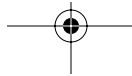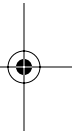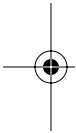
5. Using the tight binding model, find an expression for the electronic energy levels of an armchair nanotube. Make an explicit application of your expression to a (10,10) nanotube.

6. For very small-diameter nanotubes, at what diameter does the tube curvature impose sp^3 bonding rather than sp^2 bonding. Explain in what sense we can consider this cross-over point to indicate that the graphitic nanotube becomes a nanodiamond.

7. Find the electronic energy levels for a free electron nanowire with a square cross section (a^2) and a length $10a$. At what temperature would you expect quantum confinement effects to become important at room temperature?

8. Find the electronic energy levels of a silicon nanowire of diameter d_w with its wire axis along (100) and then repeat for its wire axis along (111). Use the effective mass approximation and effective mass tensor components for 3-D Si. Explain how to find the effective mass that governs transport along the nanowire axis and how to find the threshold for optical transitions.

9. Assume that the carriers of a nanowire of diameter d_w have an effective mass of $0.1m_0$ in the plane of the nanowire and $0.05m_0$ along the nanowire axis. At what magnetic field value would the electron scattering rate for carriers in a nanowire of diameter d_w decrease rapidly for a magnetic field parallel to the nanowire axis? Repeat for the case of a magnetic field perpendicular to the wire axis.

10. Consider a silicon nanowire to be the same as in Problem 7. At what magnetic field along the nanowire axis is the spacing of the Landau levels (magnetic energy levels) equal to the subband spacing? Explain why carrier localization is expected as the nanowire cross-sectional area becomes very small.

REFERENCES

1. Dresselhaus, M.S., Dresselhaus, G., and Eklund, P.C., *Science of Fullerenes and Carbon Nanotubes,* Academic Press, New York, San Diego, CA, 1996.
2. Dresselhaus, M.S., Dresselhaus, G., and Avouris, Ph., *Carbon Nanotubes: Synthesis, Structure, Properties and Applications,* Vol. 80 of *Springer Series in Topics in Appl. Phys,* Springer-Verlag, Berlin, 2001.
3. Harris, P., *Carbon Nanotubes and Related Structures: New Materials for the Twenty-First Century,* Cambridge University Press, Cambridge, UK, 2001.
4. Bandow, S., Hiraoka, K., Chen, G., Eklund, P.C., and Iijima, S., Turning Peapods into Double Walled Carbon Nanotubes. *Bulletin Mater. Res. Soc., 29,* 260–264, 2004.
5. Saito, R., Dresselhaus, G., and Dresselhaus, M.S., *Physical Properties of Carbon Nanotubes,* Imperial College Press, London, 1998.
6. Dresselhaus, M.S., Dresselhaus, G., Charlier, J.C., and Hernández, E., Electronic, thermal and mechanical properties of carbon nanotubes. Terrones, M., Ed., in *Philosophical Transactions of the Royal Society, A, 362,* 2065–2098, Royal Society, Oxford, UK, 2003.
7. Hamada, N., Sawada, S., and Oshiyama, A., *Phys. Rev. Lett., 68,* 1579–1581, 1992.

8. Saito, R., Fujita, M., Dresselhaus, G., and Dresselhaus, M.S., *Appl. Phys. Lett.*, *60,* 2204–2206, 1992.
9. Mintmire, J.W., Dunlap, B.I., and White, C.T., *Phys. Rev. Lett.*, *68,* 631–634, 1992.
10. Samsonidze, Ge.G., Grüneis, A., Saito, R., Jorio, A., Souza Filho, A.G., Dresselhaus, G., and Dresselhaus, M.S., *Phys. Rev. B, 69,* 205402, 1–11, 2004.
11. Samsonidze, Ge.G., Saito, R., Jorio, A., Pimenta, M.A., Souza Filho, A.G., Grüneis, A., Dresselhaus, G., and Dresselhaus, M.S., *J. Nanosci. Nanotechnol.*, *3,* 431–458, 2003.
12. Chico, L., Crespi, V.H., Benedict, L.X., Louie, S.G., and Cohen, M.L., *Phys. Rev. Lett.*, *76,* 971–974, 1996.
13. Liu, J., Fan, S., and Dai, H., *Bulletin Mater. Res. Soc., 29,* 244–250, 2004.
14. Bethune, D.S., Kiang, C.H., de Vries, M.S., Gorman, G., Savoy, R., Vazquez, J., and Beyers, R., *Nature* (London)*, 363,* 605, 1993.
15. Journet, C., Maser, W.K., Bernier, P., Loiseau, A., Lamy de la Chapelle, M., Lefrant, S., Deniard, P., Lee, R., and Fischer, J.E., *Nature* (London), 388, 756–758, 1997.
16. Thess, A., Lee, R., Nikolaev, P., Dai, H., Petit, P., Robert, J., Xu, C., Lee, Y.H., Kim, S.G., Rinzler, A.G., Colbert, D.T., Scuseria, G.E., Tománek, D., Fischer, J.E., and Smalley, R.E., *Science, 273,* 483–487, 1996.
17. Nilolaev, A.V., Bronikowski, M.J., Bradley, R.K., Rohmund, F., Colbert, D.T., Smith, K.A., and Smalley, R.E., *Chem. Phys. Lett.*, *313,* 91–97, 1999.
18. Maruyama, S., *Physica B, 323,* 193–195, (2002).
19. Hayashi, T., Kim, Y.A., Matoba, T., Esaka, M., Nishimura, K., Endo, M., and Dresselhaus, M.S., *Nano Lett.*, *3,* 887–889, 2003.
20. Kitiyanan, B., Alvarez, W.E., Harwell, J.H., and Resasco, D.E., *Chem. Phys. Lett.*, *317,* 497, 2000.
21. Alvarez, W.E., Kitiyanan, B., Borgna, A., and Resasco, D.E., *Carbon, 39,* 547, 2001.
22. Haddon, R.C., Sippel, J., Rinzler, A.G., and Papadimitrakopoulos, F., *Bulletin Mater. Res. Soc., 29,* 252–259, 2004.
23. Liu, K., Chien, C.L., and Searson, P.C., *Phys. Rev. B, 58,* R14681–R14684, 1998.
24. Rinzler, A.G., Liu, J., Dai, H., Nikolaev, P., Huffman, C.B., and Rodriguez-Marcias, F.J., *Appl. Phys. A, 67,* 29–37, 1998.
25. Chattopadhyay, D., Galeska, I., and Papadimitrakopoulos, F., *Carbon, 40,* 985–988, 2002.
26. Endo, M., Kim, Y.A., Fukai, Y., Hayashi, T., Terrones, M., Terrones, H., and Dresselhaus, M.S., *Appl. Phys. Lett., 79,* 1531–1533, 2001.
27. Endo, M., Hayashi, T., Kim, Y.A., Terrones, M., and Dresselhaus, M.S., in Ferrari, A. and Robertson, J. Eds. "Application of Carbon Nanotubes in the XXI Century." Vol 362, 2223–2238. *Philosophical Transactions of the Royal Society: Special Issue; Raman Spectroscopy in Carbons: From Nanotubes to Diamond*, Royal Society, Oxford, UK, 2004.
28. Chattopadhyay, D., Galeska, I., and Papadimitrakopoulos, F., *J. Am. Chem. Soc., 125,* 3370–3375, 2003.
29. Zheng, M., Jagota, A., Semke, E.D., Diner, B.A., McLean, R.S., Lustig, S.R., Richardson, R.E., and Tassi, N.G., *Nature Mater., 2,* 338–342, 2003.
30. Zheng, M., Jagota, A., Strano, M.S., Barone, P., Chou, S.G., Diner, B.A., Dresselhaus, M.S., McLean, R.S., Onoa, G.B., Santos, A.P., Semke, E.D., Usrey, M., and Walls, D.J., *Science, 302,* 1545–1548, 2003.
31. Lebedkin, S., Arnold, K., Hennrich, F., Krupke, R., Renker, B., and Kappes, M.M., *New J. Phys., 5,* 140, 2003.
32. Strano, M.S., *J. Am. Chem. Soc.*, *125,* 16148–16153, 2003.

33. Strano, M.S., Miller, M.K., Allen, M.J., Moore, V.C., O'Connell, M.J., Kittrell, C., Hauge, R.H., and Smalley, R.E., *J. Nanosci. Nanotechnol., 3,* 81–86, 2003.
34. Strano, M.S., *J. Am. Chem. Soc ., 125,* 16148–16150 (2004).
35. Chen, G., Sumanasekera, G.U., Pradhan, B.K., Gupta, R., Eklund, P.C., Bronikowski, M.J., and Smalley, R.E., *J. Nanosci. Nanotech ., 2,* 621–626, 2002.
36. Kataura, H., Kimura, A., Ohtsuka, Y., Suzuki, S., Maniwa, Y., Hanyu, T., and Achiba, Y., *Jpn. J. Appl. Phys. Pt.2-Letters, 37,* L616–L618, 1998.
37. Hagen, A., and Hertel, T., *Nanoletters, 3,* 383–388, 2003.
38. Rao, A.M., Richter, E., Bandow, S., Chase, B., Eklund, P.C., Williams, K.W., Fang, S., Subbaswamy, K.R., Menon, M., Thess, A., Smalley, R.E., Dresselhaus, G., and Dresselhaus, M.S., *Science, 275,* 187–191, 1997.
39. Dresselhaus, M.S., Dresselhaus, G., Jorio, A., Souza Filho, A.G., and Saito, R., *Carbon, 40,* 2043–2061, 2002.
40. O'Connell, M.J., Bachilo, S.M., Huffman, X.B., Moore, V.C., Strano, M.S., Haroz, E.H., Rialon, K.L., Boul, P.J., Noon, W.H., Kittrell, C., Ma, J., Hauge, R.H., Weisman, R.B., and Smalley, R.E., *Science, 297,* 593–596, 2002.
41. Jorio, A., Saito, R., Hafner, J.H., Lieber, C.M., Hunter, M., McClure, T., Dresselhaus, G., and Dresselhaus, M.S., *Phys. Rev. Lett ., 86,* 1118–1121, 2001.
42. Dresselhaus, M.S., and Eklund, P.C., *Advan. Phys ., 49,* 705–814, 2000.
43. Pimenta, M.A., Marucci, A., Empedocles, S., Bawendi, M., Hanlon, E.B., Rao, A.M., Eklund, P.C., Smalley, R.E., Dresselhaus, G., and Dresselhaus, M.S., *Phys. Rev. B Rapid, 58,* R16016–R16019, 1998.
44. Brown, S.D.M., Jorio, A., Corio, P., Dresselhaus, M.S., Dresselhaus, G., Saito, R., and Kneipp, K., *Phys. Rev. B, 63,* 155414, 2001.
45. Jorio, A., Dresselhaus, G., Dresselhaus, M.S., Souza, M., Dantas, M.S.S., Pimenta, M.A., Rao, A.M., Saito, R., Liu, C., and Cheng, H.M., *Phys. Rev. Lett ., 85,* 2617–2620, 2000.
46. Jorio, A., Pimenta, M.A., Souza Filho, A.G., Samsonidze, Ge.G., Swan, A.K., Ünlü, M.S., Goldberg, B.B., Saito, R., Dresselhaus, G., and Dresselhaus, M.S., *Phys. Rev. Lett., 90,* 107403, 2003.
47. Thomsen, C., and Reich, S., *Phys. Rev. Lett., 85,* 5214, 2000.
48. Souza Filho, A.G., Jorio, A., Samsonidze, Ge.G., Dresselhaus, G., Dresselhaus, M.S., Swan, A.K., Ünlü, M.S., Goldberg, B.B., Saito, R., Hafner, J.H., Lieber, C.M., and Pimenta, M.A., *Chem. Phys. Lett., 354,* 62–68, 2002.
49. Saito, R., Dresselhaus, G., and Dresselhaus, M.S., *Phys. Rev., B, 61,* 2981–2990, 2000.
50. Samsonidze, Ge.G., Saito, R., Jorio, A., Souza Filho, A.G., Grüneis, A., Pimenta, M.A., Dresselhaus, G., and Dresselhaus, M.S., *Phys. Rev. Lett., 90,* 027403, 2003.
51. Kataura, H., Kumazawa, Y., Maniwa, Y., Umezu, I., Suzuki, S., Ohtsuka, Y., and Achiba, Y., *Synthe. Met ., 103,* 2555–2558, 1999.
52. Souza Filho, A.G., Chou, S.G., Samsonidze, Ge.G., Dresselhaus, G., Dresselhaus, M.S., Lei An, J. Liu, Anna Swan, K., Ünlü, M.S., Goldberg, B.B., Jorio, A., Grüneis, A., and Saito, R., *Phys. Rev. B, 69,* 115428, 2004.
53. Jorio, A. , Souza Filho, A.G., Dresselhaus, G., Dresselhaus, M.S., Saito, R., Hafner, J.H., Lieber, C.M., Matinaga, F.M., Dantas, M.S.S., and Pimenta, M.A., *Phys. Rev. B, 63,* 245416, 1–4, 2001.
54. Fantini, C., Jorio, A., Souza, M., Mai Jr., A.J., Strano, M.S., Dresselhaus, M.S., and Pimenta, M.A., *Phys. Rev. Lett., 93,* 147406 (2004).
55. Cronin, S.B., Barnett, R., Tinkham, M., Chou, S.G., Rabin, O., Dresselhaus, M.S., Swan, A.K., Ünlü, M.S., and Goldberg, B.B., *Appl. Phys. Lett., 84,* 2052–2055, 2004. Also *Virtual J. Nanoscale Sci. Technol.,* 2004.

56. Lin, Yu-Ming, and Dresselhaus, M.S., *Appl. Phys. Lett., 83,* 3567–3569, 2003.
57. Fantini, C., Jorio, A., Souza, M., Ladeira, L.O., Pimenta, M.A., Souza Filho, A.G., Saito, R., Samsonidze, Ge.G., Dresselhaus, G., and Dresselhaus, M.S., *Phys. Rev. Lett., 93,* 087401 (2004).
58. Dresselhaus, G., Pimenta, M.A., Saito, R., Charlier, J.-C, Brown, S.D.M., Corio, P., Marucci, A., and Dresselhaus, M.S. "On the π–π Overlap Energy in Carbon Nanotubes." In Tománek, D. and Enbody, R.J., *Science and Applications of Nanotubes,* 275–295, Kluwer Academic, New York, 2000. Proceedings of the International Workshop on the Science and Applications of Nanotubes, Michigan State University, East Lansing, MI, July 24–27, 1999.
59. Hartschuh, A., Sanchez, E.J., Xie, X.S., and Novotny, L., *Phys. Rev. Lett., 90,* 95503, 2003.
60. Hartschuh, A., Pedrosa, H.N., Novotny, L., and Krauss, T.D., *Science, 301,* 1354–1356, 2003.
61. Saito, R., and Kataura, H. "Optical Properties," in *Carbon Nanotubes: Synthesis, Structure, Properties and Applications,* Dresselhaus, M.S., Dresselhaus, G., and Avouris, P. Eds., pp. 213–246, Springer Series in Topics in Applied Physics, Vol. 80, Spring-Verlag, Berlin, 2001.
62. Kuzmany, Hans, *Solid-State Spectroscopy: An Introduction*, Springer-Verlag, Berlin, 1998, Vol. 50, p. 115. See Section 6.3.3 "Oscillator Strength and Sum Rules."
63. Sen, R., Rickard, S.M., Itkis, M.E., and Haddon, R.C., *Chem. Mater., 15,* 4273, 2003.
64. Hertel, T., and Moos, G., *Chem. Phys. Lett., 320,* 359–364, 2000.
65. Hertel, T., and Moos, G., *Phys. Rev. Lett., 84,* 5002–5005, 2000.
66. Bachilo, S.M., Strano, M.S., Kittrell, C., Hauge, R.H., Smalley, R.E., and Weisman, R.B., *Science, 298,* 2361–2366, 2002.
67. Weisman, R.B., and Bachilo, S.M., *Nanoletters, 3,* 1235–1238, 2003.
68. Niyogi, S., Hamon, M.A., Hu, H., Zhao, B., Bhowmik, P., Sen, R., Itkis, M.E., and Haddon, R.C., *Acc. Chem. Res., 35,* 1105–1113, 2002.
69. Feynman, Richard P. (1959). From a talk reported at http://www.zyvex.com/nanotech/feynman.html.
70. Dresselhaus, M.S., Lin, Y.-M., Rabin, O., Black, M.R., and Dresselhaus, G., Nanowires, in Bhushan, B., Ed., *Springer Handbook of Nanotechnology,* pp. 99–145, Springer-Verlag, Heidelberg, Germany, 2004.
71. Dresselhaus, M.S., Lin, Yu-Ming, Cronin, S.B., Rabin, O., Black, M.R., Dresselhaus, G., and Koga, T. "Quantum Wells and Quantum Wires for Potential Thermoelectric Applications," in *Semiconductors and Semimetals: Recent Trends in Thermoelectric Materials Research III,* Tritt, T. M., pp. 1–121, Academic Press, San Diego, 2001.
72. Heremans, J., "Thermoelectric Power, Electrical and Thermal Resistance and Magnetoresistance of Nanowire Composites," in *Thermoelectric Materials 2003—Research and Applications: MRS Symposium Proceedings, Boston, December 2003*, Nolas, G.S., Yang, J., Hogan, T.P., and Johnson, D.C., Eds., pp. 3–14, Materials Research Society Press, Pittsburgh, 2004.
73. Whitney, T.M., Jiang, J.S., Searson, P.C., and Chien, C.L., *Science, 261,* 1316, 1993.
74. Piraux, L., Dubois, S., Duvail, J.L., and Radulescu, A., *J. Mater. Res., 14,* 3042–3050, 1999.
75. Rabin, Oded, *Bismuth Nanowire and Antidot Array Studies Motivated by Thermoelectricity,* Ph.D. thesis, Massachusetts Institute of Technology, Department of Chemistry, June 2004.
76. Huber, C.A., Huber, T.E., Sadoqi, M., Lubin, J.A., Manalis, S., and Prater, C.B., *Science, 263,* 800–802, 1994.

77. Zhang, Z., Ying, J.Y., and Dresselhaus, M.S., *J. Mater. Res., 13,* 1745–1748, 1998.

78. Lin, Y.-M., Cronin, S.B., Ying, J.Y., Dresselhaus, M.S., and Heremans, J.P., *Appl. Phys. Lett., 76,* 3944–3946, 2000.

79. Adamson, A.W., *Physical Chemistry of Surfaces* , Wiley, New York, 1982, p. 338.

80. Zhang, Z., Gekhtman, D., Dresselhaus, M.S., and Ying, J.Y., *Chem. Mater., 11,* 1659–1665, 1999.

81. Huber, T.E., Graf, M.J., Foss, Jr., C.A., and Constant, P., *J. Mater. Res., 15,* 1816–1821, 2000.

82. Liu, K., Chien, C.L., Searson, P.C., and Kui, Y.Z., *Appl. Phys. Lett., 73,* 1436–1438, 1998.

83. Almawlawi, D., Liu, C.Z., and Moskovits, M., *J. of Mater. Res., 9,* 1014–1018, 1994.

84. Sapp, S.A., Lakshmi, B.B., and Martin, C.R., *Adv. Mater., 11,* 402–404, 1999.

85. Prieto, A.L., Sander, M.S., Martin-Gonzalez, M.S., Gronsky, R., Sands, T., and Stacy, A.M., *J. Am. Chem. Soc., 123,* 7160–7161, 2001.

86. Sander, M.S., Gronsky, R., Sands, T., and Stacy, A.M., *Chem. Mater., 15,* 335–339, 2003.

87. Yin, A.J., Li, J., Jian, W., Bennett, A.J., and Xu, J.M., *Appl. Phys. Lett., 79,* 1039–1041, 2001.

88. Peng, Xiaogang, Manna, Liberato, Yang, Weidong, Wickham, Juanita, Scher, Erik, Kadavanich, Andreas, and Alivisatos, A.P., *Nature, 404,* 59–61, 2000.

89. Jin, C.G., Jiang, G.W., Liu, W.F., Cai, W.L., Yao, L.Z., Yao, Z., and Li, X.G., *J. Mater. Chem., 13,* 1743–1746, 2003.

90. Toimil Molares, M.E., Chtanko, N., Cornelius, T.W., Dobrev, D., Enculescu, I., Blick, R.H., and Neumann, R., *Nanotechnology, 15,* S201–S207, 2004.

91. Rabin, O., Chen, G., and Dresselhaus, M.S., *The Electrochemical Society Meeting Abstracts, 2003-02,* Abs. 25, 2003.

92. Heremans, J., Thrush, C.M., Lin, Yu-Ming, Cronin, S., Zhang, Z., Dresselhaus, M.S., and Mansfield, J.F., *Phys. Rev. B, 61,* 2921–2930, 2000.

93. Rabin, O., Herz, P.R., Lin, Y.-M., Akinwande, A.I., Cronin, S.B., and Dresselhaus, M.S., *Adv. Funct. Mater., 13,* 631–638, 2003.

94. Yu-Ming, Lin., *Thermoelectric Properties of Bi $_{1-x}$Sb$_x$ and Superlattice Nanowires,* Ph.D. thesis, Massachusetts Institute of Technology, Department of Electrical Engineering and Computer Science, June 2003.

95. Cronin, S.B., Lin, Y.-M., Rabin, O., Black, M.R., Dresselhaus, G., Dresselhaus, M.S., and Gai, P.L., *Microscopy and Microanalysis, 8,* 58–63, 2002.

96. Sander, M.S., Gronsky, R., Lin, Y.-M., and Dresselhaus, M.S., *J. Appl. Phys., 89,* 2733–2736, 2001.

97. Cronin, S.B., Lin, Y.-M., Rabin, O., Black, M.R., Ying, J.Y., Dresselhaus, M.S., Gai, P.L., Minet, J.-P., and Issi, J.-P., *Nanotechnology J., 13,* 653–658, 2002.

98. Cronin, Stephen B., *Electronic Properties of Bi Nanowires,* Ph.D. thesis, Massachusetts Institute of Technology, Department of Physics, June 2002.

99. Hong, K., Yang, F.Y., Liu, K., Reich, D.H., Searson, P.C., and Chien, C.L., *J. Appl. Phys., 85,* 6184–6186, 1999.

100. Lin, Y.-M., Sun, X., and Dresselhaus, M.S., *Phys. Rev. B, 62,* 4610–4623, 2000.

101. Rabin, O., Lin, Yu-Ming, and Dresselhaus, M.S., *Appl. Phys. Lett., 79,* 81–83, 2001.

102. Lin, Y.-M., Rabin, O., Cronin, S.B., Ying, J.Y., and Dresselhaus, M.S., *Appl. Phys. Lett., 81,* 2403–2405, 2002.

103. Lin, Y.-M., Rabin, O., Cronin, S.B., Ying, J.Y., and Dresselhaus, M.S., in Caillat, T., and Snyder, J. "Experimental Investigation of Thermoelectric Properties of BiSb Nanowire Arrays." *The 21st International Conference on Thermoelectrics: ICT*

Symposium Proceedings, Long Beach, CA, pp. 253–256, Institute of Electrical and Electronics Engineers, Inc., Piscataway, NJ, 2002.

104. Black, Marcie R., *The Optical Properties of Bi Nanowires,* Ph.D. thesis, Massachusetts Institute of Technology, Department of Electrical Engineering and Computer Science, June 2003.

105. Black, M.R., Hagelstein, P.L., Cronin, S.B., Lin, Y.-M., and Dresselhaus, M.S., *Phys. Rev. B, 68,* 235417, 2003.

106. Dresselhaus, M.S., Lin, Y.-M., Rabin, O., Jorio, A., Souza Filho, A.G., Pimenta, M.A., Saito, R., Samsonidze, Ge.G., and Dresselhaus, G., *Mater. Sci. Engin. C, 23,* 129–140, 2003.